

# 2D and 3D High Frame Rate Imaging with Limited Diffraction Beams

Jian-yu Lu, *Member, IEEE*

**Abstract**—A new 2D (two-dimensional) and 3D (three-dimensional) pulse-echo imaging method (Fourier method) has been developed with limited diffraction beams. In this method, a plane wave pulse (broadband) is used to transmit and limited diffraction beams of different parameters are used to receive. Signals received are processed to obtain spatial Fourier transform of object functions and images are constructed with an inverse Fourier transform. Because only one transmission is required to construct images, this method may achieve a high frame rate (up to 3750 frames/s for biological soft tissues at a depth of 200 mm). To demonstrate the efficacy of the method, both 2D C-mode and 3D images have been simulated using conditions that are typical for medical ultrasound. Results show that images of high resolutions (about 6 wavelengths at 200 mm) and low sidelobes (around  $-60$  dB) can be constructed over a large depth of interest (30 to 200 mm) with a 50 mm diameter aperture. Experiments with the new method have also been carried out. 2D B-mode images have been constructed with conventional linear arrays. In the experiment, an ATS 539 tissue-equivalent phantom and two linear arrays were used. The first array had a center frequency of 2.25 MHz, dimension of  $18.288 \text{ mm} \times 12.192 \text{ mm}$ , and 48 elements. The second had a center frequency of 2.5 MHz,  $38.4 \text{ mm} \times 10 \text{ mm}$  in dimension, and 64 elements. Images of different fields of views were constructed from RF data acquired with these arrays using both the new and conventional dynamic focusing (delay-and-sum) methods. Results show that qualities of images constructed are almost identical with the two methods in terms of sidelobes, contrast, and lateral and axial resolutions. Phase aberration has also been assessed for the two methods, and results show that its influence is about the same on both methods. In addition, a practical imaging system to implement the new method is suggested and potential applications of the method are discussed.

## I. INTRODUCTION

LIMITED DIFFRACTION BEAMS were first discovered by Stratton in 1941 [1] where he derived a Bessel beam solution to the isotropic-homogeneous wave equation. In 1987, Durnin [2] and Durnin *et al.* [3] studied the Bessel beam again and produced the beam approximately with an optical experiment. Durnin has termed Bessel beams “non-diffracting” or “diffraction-free” beams. Because Durnin’s terminologies are controversial, the new terminology “limited diffraction beams” has been used in recent years

[4]. The new terminology is based on the fact that any practical beams will diffract eventually. Limited diffraction beams have an interesting feature: theoretically, these beams can propagate to an infinite distance without changing their transverse beam patterns. In practice, when produced with a finite-aperture radiator, these beams have a large depth of field as compared to conventional spherically focused beams. Because of this property, limited diffraction beams such as Bessel beams have been studied by many other investigators in optics, microwave, and acoustics [5]–[12]. In addition, limited diffraction beams have been studied for both medical and nonmedical applications, such as, medical imaging [4], [13]–[18], tissue characterization [19], transverse Doppler velocity measurement [20], [21], high-speed digital wireless telecommunications [22], and nondestructive evaluation of industrial materials [23]. Recently, a new class of limited diffraction beams such as X waves [24]–[28], limited diffraction array beams [29]–[31], and bowtie limited diffraction beams [13]–[14], have been developed and their theories have been studied extensively [32]–[34].

In addition to limited diffraction beams, localized waves are another class of beams that have a large depth of field. Localized waves were first discovered by Brittingham in 1983 [35] and were further studied by Ziolkowski [36] and Ziolkowski *et al.* [37] and many other investigators [38], [39]. These waves deform as they propagate but have lower sidelobes than limited diffraction beams such as Bessel beams and X waves. However, when localized waves are produced with a finite bandwidth that is realizable with a medical ultrasound transducer, their sidelobes are as high as those of Bessel beams and X waves [4], [40].

In this paper, a new method (Fourier method) [20], [41] for high frame rate 2D (two-dimensional) B-mode (image plane is defined by transducer and its beam axis), 2D C-mode (image plane is in parallel with transducer surface), and 3D (three-dimensional) pulse-echo imaging has been developed with limited diffraction beams [15], [24], specifically, with limited diffraction array beams [29]–[31]. In this method, a plane wave pulse (broadband) is transmitted from a 2D (for 2D C-mode and 3D imaging) or 1D (for 2D B-mode imaging) array transducer to uniformly illuminate objects to be imaged, and echoes returned from the objects are received with the same transducer but weighted to produce limited diffraction responses. The received signals are used to calculate the Fourier transform of the object to be imaged. Object functions (reflectivity coefficients) are constructed with a 2D (for 2D imaging) or 3D (for 3D imaging) inverse spatial Fourier transform. In

Manuscript received August 13, 1996; accepted February 18, 1997. This work was supported in part by grants CA 54212 and CA 43920 from the National Institutes of Health.

The author is with the Department of Physiology and Biophysics, Mayo Clinic and Foundation, Rochester, MN 55905 (e-mail: jian@mayo.edu).

the image construction, the entire transducer aperture is used and both the transmission and reception beams do not diverge over a large depth of interest. This results in an imaging system of a high signal-to-noise ratio (SNR) as compared to that of conventional dynamically focused systems. Because only one transmission is required to construct 2D or 3D images, in theory, this method can achieve a maximum frame rate of about 3750 frames/second for imaging of biological soft tissues at a depth of 200 mm. In addition, the Fourier and inverse Fourier transforms can be implemented with FFT (fast Fourier transform) and IFFT (inverse fast Fourier transform) algorithms that can be realized with modern DSP (digital signal processing) chips or ASIC (application specific integrated circuit) resulting in simple and inexpensive imaging systems as compared to conventional dynamically focused digital beam formers. With the new method, beam steering is not necessary. However, electronic steering of beams can also be applied to increase the field of view of images. Because of high frame rate, speckle tracking technique [42] may be better applied with the new method to obtain either 2D or 3D blood flow velocity vectors. Underwater acoustic imaging in high frame rate is also possible with the new method [43]. Moreover, theory of the new method can be extended to other data acquisition geometries to improve image quality (see Discussion).

Several methods have been developed in the past that either increase image frame rate or use also backscattered waves to construct 2D and 3D images. The first is a 3D imaging system developed at the Duke University where a wide transmit beam is used to illuminate an area that contains 16 to 32 conventional dynamically focused receive beams [44]–[46]. This system is limited. Firstly, the frame rate is increased at most by 32 times, which is still low for conventional imaging. For color blood flow imaging, the frame rate will be further reduced. Secondly, there must be 16 to 32 multichannel dynamic focusing beamformers to process receive signals in parallel. Although this problem was partially avoided by using one main beamformer and multiple approximate beamformers (explososcan [44]), the approximate beamformers produce phase errors that distort images of objects and degrade image quality as the receive beams scan from one angle to another. Thirdly, to cover all 16 to 32 receive beams uniformly, the transmit beam must be wide enough and thus the area of the transmit aperture is reduced by at least 16 to 32 times that in turn dramatically decrease transmit energy leading to a low SNR at deeper depths.

Other methods are based on synthetic aperture and holographic concepts [47], [48]. In these methods, diverging transmit beams are used to illuminate an object to be constructed. Received backscatter signals are processed with a delay-and-sum algorithm [49] where, for each point in the object, its distances to the elements of a receiver array are determined by arriving times of echoes, and appropriate delays are added to the receive signals so they can be summed constructively for that point. For this method to work, RF signals are required and thus a high sampling

rate is needed to avoid signal aliasing and delay quantization errors. Assume that there is a 3D object that has  $N_x \times N_y \times N_z$  points, where  $N_z$  is a large number needed to avoid aliasing, the delay-and-sum algorithm requires about  $N_x \times N_y \times N_z \times N_{x_1} \times N_{y_1}$  computations plus delay and interpolation operations, where  $N_{x_1}$  and  $N_{y_1}$  are number of elements of a 2D array in the  $x$  and  $y$  directions, respectively. This requires a huge computation power to achieve a frame rate of 3750 leading to a very complex system. In addition, the energy density of a diverging wave is inversely proportional to the square of distance, and thus the systems will have a low SNR in biological soft tissues. Ylitalo and Ermert have proposed a backpropagation Fourier method [70]. This method has a very low frame rate in 3D imaging because more than 10,000 transmissions are required to obtain a frame of image. This method also suffers from low SNR because strongly diverged transmit beams have to be used to increase lateral resolution. In addition, the method is based on holographic concept, where monochromatic illumination is desirable which reduces axial resolution of images. Methods for 3D real-time imaging using coded transmissions and matrix inversions have also been proposed [50]. These methods require a complex data acquisition system and suffer from problems similar to the delay-and-sum (a large amount of computations) method.

It is worth noting that construction of images from backscattered signals has also been studied by many investigators [51]–[53]. Norton and Linzer [51] have suggested using a point source on a 2D surface to transmit and receive sequentially to construct images. As discussed above, this method suffers from low frame rate and low SNR and thus is not suitable for the study of biological soft tissues for a valid medical diagnosis. Ultrasound tomography can also be used to construct images with backscattered signals. However, it requires transducers to rotate  $360^\circ$  around the body [54], [55]. This limits its application because of acoustic obstructions in the human body. In addition, tomography is slow, systems are complex, and images may suffer from misalignment problems due to significant changes of speed of sound at different viewing angles.

To demonstrate the efficacy of the new method developed in this paper, 2D C-mode and 3D images are simulated using conditions that are typical for conventional medical ultrasonic B-scan imaging. In the simulations, a 50 mm diameter 2D array transducer is assumed. The transducer has a center frequency of 2.5 MHz and a bandwidth of about 81% of the center frequency. Objects imaged are assumed to be composed of point scatterers embedded in a uniform background medium such as water. Images at 3 axial distances (30, 100, and 200 mm) are constructed. Results show that high-resolution (about 6 wavelengths at 200 mm) and low-sidelobe (around  $-60$  dB) images can be obtained under these conditions. In addition, a 3D imaging system to implement the method is suggested. The system is similar to conventional B-scanners from the operation point of view (pulse-echo mode) but has a completely different beamformer that can be realized

with simple and inexpensive hardware and has a potential to achieve a much higher frame rate.

Recently, an experiment for the new method has been carried out on an ATS 539 tissue-equivalent phantom (ATS Laboratories, Inc., Bridget Port, CT, USA) using two linear arrays [56]. The phantom has a frequency-dependent attenuation of about 0.5 dB/MHz/cm. The first array has a center frequency of 2.25 MHz, dimension of 18.288 mm × 12.192 mm, and 48 elements. The second has a center frequency of 2.5 MHz, 38.4 mm × 10 mm in dimension, and 64 elements. Images of different fields of views were constructed with RF data acquired with these arrays using both the new and conventional dynamic focusing (delay-and-sum) methods [49]. Results show that qualities of images constructed are almost identical with the two methods in terms of sidelobes, contrast, and lateral and axial resolutions. Influence of phase aberration has also been studied for the two methods, and results show that it is about the same on both methods [57].

This paper is organized as follows. In Section II, theoretical formulas of the new imaging method are derived with limited diffraction beams. 2D and 3D images of several objects are simulated in Section III, and results are presented in Section IV. A suggested system to implement the new method is given in Section V. Extension of theory and discussions of the method are in Section VI. Finally, brief summary and conclusion are given in Section VII.

## II. THEORY

In this section, a new imaging method (Fourier method) for a pulse-echo system will be developed and formulas for construction of 2D and 3D images will be derived from limited diffraction beams.

### A. Derivation of Limited Diffraction Array Beams from X Waves

In the following, broadband limited diffraction array beams [29]–[31] will be first derived using X waves [24], [25] that have been extensively studied in the past few years and their properties are well understood.

The equation for X waves may be expressed as follows (see (12) in [24]):

$$\begin{aligned}\Phi_{X_n}(\vec{r}, t) &= \Phi_{X_n}(r, \phi, z - c_1 t) \\ &= e^{in\phi} \int_0^\infty B(k) J_n(kr \sin \zeta) e^{-k[a_0 - i \cos \zeta (z - c_1 t)]} dk, \\ &\quad (n = 0, 1, 2, \dots),\end{aligned}\quad (1)$$

where  $\vec{r} = (r, \phi, z)$  represents a spatial point in the cylindrical coordinates,  $t$  is time,  $r$  is radial distance,  $\phi$  is polar angle,  $z$  is the axial distance,  $c_1 = c/\cos \zeta$  is the phase velocity of X waves,  $k = \omega/c$  is the wave number,  $\omega = 2\pi f$  is the angular frequency,  $f$  is the temporal frequency,  $c$  is the speed of sound or light,  $\zeta$  ( $0 \leq \zeta < \pi/2$ ) is the Axicon

angle [58], [59] of X waves,  $J_n(\cdot)$  is the  $n$ th-order Bessel function of the first kind,  $B(k)$  is any well-behaved function that could represent the transfer function of a practical acoustic transducer or electromagnetic antenna, and  $a_0$  is a constant that determines the fall-off speed of the high-frequency components of X waves, and  $n$  is termed the “order” of the waves.

With an infinite aperture, X waves can propagate to an infinite distance without changing their wave shapes. If the aperture is finite, these waves have a large depth of field [24], [25]. For example, if the diameter of the aperture is  $D$ , the depth of field of the waves is given as follows [24], [30]

$$Z_{\max} = \frac{D}{2} \frac{1}{\sqrt{\left(\frac{c_1}{c}\right)^2 - 1}} = \frac{D}{2} \cot \zeta. \quad (2)$$

If  $D = 50$  mm and  $\zeta = 6.6^\circ$ , the depth of field is about 216 mm (the depth of field is defined as the axial distance from the surface of transducer where the peak pressure of the wave drops to  $-6$  dB of that at the surface).

Summing the X waves in (1) over the index,  $n$ , broadband limited diffraction array beams [29]–[31] are obtained that are also limited diffraction solutions to the isotropic-homogeneous wave equation:

$$\begin{aligned}\Phi_{\text{Array}}(\vec{r}, t) &= \sum_{n=-\infty}^{\infty} i^n e^{-in\theta} \Phi_{X_n}(r, \phi, z - c_1 t) \\ &= \int_0^\infty B(k) \left[ \sum_{n=-\infty}^{\infty} i^n J_n(kr \sin \zeta) e^{in(\phi-\theta)} \right] \\ &\quad \times e^{-k[a_0 - i \cos \zeta (z - c_1 t)]} dk,\end{aligned}\quad (3)$$

where  $0 \leq \theta < 2\pi$  is a free parameter and the subscript “Array” represents “array beams.” Because of the following equality [60],

$$\sum_{n=-\infty}^{\infty} i^n J_n(kr \sin \zeta) e^{in(\phi-\theta)} = e^{i(kr \sin \zeta) \cos(\phi-\theta)}, \quad (4)$$

the array beams can be written as [29]:

$$\begin{aligned}\Phi_{\text{Array}}(\vec{r}, t) &= \frac{1}{2\pi} \int_0^\infty T(k) e^{ik_x x + ik_y y + ik_z z} e^{-i\omega t} dk \\ &= \frac{1}{2\pi} \int_{-\infty}^\infty T(k) H(k) e^{ik_x x + ik_y y + ik_z z} e^{-i\omega t} dk,\end{aligned}\quad (5)$$

where

$$\frac{T(k) H(k)}{c} e^{ik_x x + ik_y y + ik_z z}, \quad (6)$$

is the Fourier transform (spectrum) of the array beams in terms of time,

$$H\left(\frac{\omega}{c}\right) = \begin{cases} 1, & \omega \geq 0 \\ 0, & \omega < 0 \end{cases} \quad (7)$$

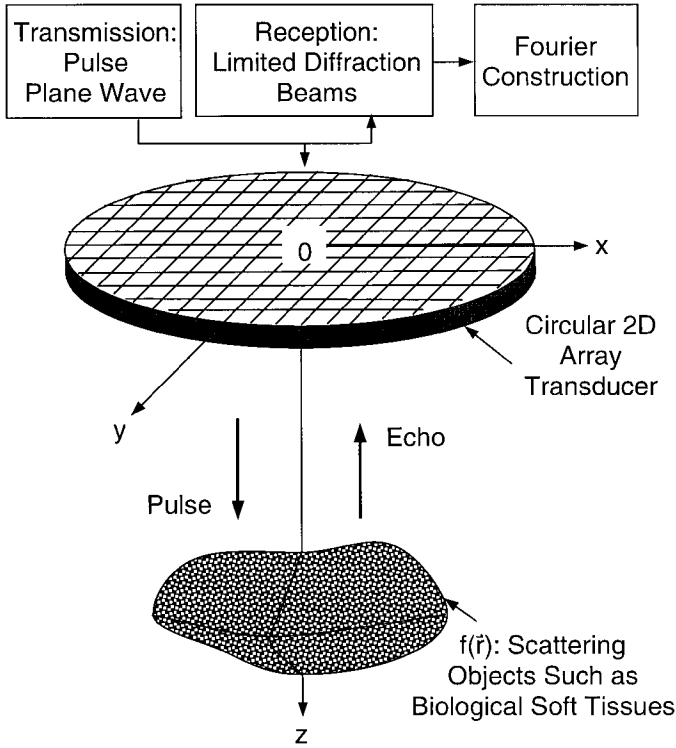


Fig. 1. Geometry of a 3D pulse-echo imaging system with limited diffraction beams.

is the Heaviside step function [61],  $T(k) = 2\pi B(k)e^{-ka_0}$ , and

$$\begin{cases} k_x = k \sin \zeta \cos \theta = k_1 \cos \theta, \\ k_y = k \sin \zeta \sin \theta = k_1 \sin \theta, \\ k_z = k \cos \zeta = \sqrt{k^2 - k_1^2} \geq 0, \end{cases} \quad (8)$$

and where

$$k_1 = \sqrt{k_x^2 + k_y^2} = k \sin \zeta. \quad (9)$$

### B. Approximate Constructions of Images with a Pulse-Echo System

In the following discussion the relationship between the signals backscattered from an object and a 3D or 2D image reconstruction of the object is established using the broadband limited diffraction array beams (5). Although the exact array beams as set forth in (5) and the use of an infinite aperture are assumed in the derivation, good images can be constructed using a transducer with a finite aperture within the depth of field of the beams (2).

*1. 3D Image Construction:* Let's assume that a 3D object,  $f(\vec{r})$  (reflection coefficient), is composed of randomly positioned point scatterers embedded in a uniform background supporting a constant speed of sound (Fig. 1) and a broadband circular 2D array transducer is excited to produce a plane wave pulse (broadband) that is expressed as follows (derived from (4) of [24])

$$\begin{aligned} P(z - ct) &= \frac{1}{2\pi} \int_{-\infty}^{\infty} A(k) e^{ik(z-ct)} dk \\ &= \frac{1}{2\pi} \int_{-\infty}^{\infty} A(k) e^{ikz} e^{-i\omega t} dk, \end{aligned} \quad (10)$$

where

$$\frac{A(k)e^{ikz}}{c} \quad (11)$$

is the temporal spectrum of the plane wave pulse.

If the same array transducer is used as a receiver and is weighted to produce a limited diffraction array beam response with the parameters  $k_x$  and  $k_y$ , the received signal for the wave scattered from a point scatterer located at  $\vec{r} = (x, y, z)$  is given by the following convolution [(6) and (11)]:

$$\begin{aligned} R_{k_x, k_y, k'_z}^{(\text{one})}(t) &= f(\vec{r}) [P(z - ct) * \Phi_{\text{Array}}(\vec{r}, t)] \\ &= \frac{1}{2\pi} \int_{-\infty}^{\infty} \frac{A(k)T(k)H(k)}{c} f(\vec{r}) e^{ik_x x + ik_y y + ik'_z z} \\ &\quad \times e^{-i\omega t} dk, \end{aligned} \quad (12)$$

where “\*” represents the convolution with respect to time and where  $k'_z = k + k_z$ , and the superscript “(one)” means “one point scatterer.” This uses the fact that the spectrum of the convolution of two functions is equal to the product of the spectra of the functions.

Because the imaging system is linear, the received signal for echoes returned from all random scatterers within the object  $f(\vec{r})$  is a linear superposition of those echo signals from individual point scatterers as follows:

$$\begin{aligned} R_{k_x, k_y, k'_z}(t) &= \frac{1}{2\pi} \int_{-\infty}^{\infty} \frac{A(k)T(k)H(k)}{c} \\ &\quad \times \left[ \int_V f(\vec{r}) e^{ik_x x + ik_y y + ik'_z z} d\vec{r} \right] e^{-i\omega t} dk \\ &= \frac{1}{2\pi} \int_{-\infty}^{\infty} \frac{A(k)T(k)H(k)}{c} F(k_x, k_y, k'_z) e^{-i\omega t} dk. \end{aligned} \quad (13)$$

The 3D Fourier transform pair in this expression is defined as follows:

$$F(k_x, k_y, k_z) = \int_V f(\vec{r}) e^{ik_x x + ik_y y + ik_z z} d\vec{r} \quad \text{and} \quad (14)$$

$$\begin{aligned} f(\vec{r}) &= \frac{1}{(2\pi)^3} \int_{-\infty}^{\infty} \int_{-\infty}^{\infty} \int_{-\infty}^{\infty} F(k_x, k_y, k_z) \\ &\quad \times e^{-ik_x x - ik_y y - ik_z z} dk_x dk_y dk_z, \end{aligned}$$

and where  $V$  is the volume of the object  $f(\vec{r})$ .

From (13) the temporal Fourier transform (spectrum) of the received signal is obtained:

$$\tilde{R}_{k_x, k_y, k'_z}(\omega) = \frac{A(k)T(k)H(k)}{c^2} F(k_x, k_y, k'_z) \quad (15)$$

or

$$F_{\text{BL}}(k_x, k_y, k'_z) = c^2 H(k) \tilde{R}_{k_x, k_y, k'_z}(\omega),$$

where  $H(k)$  is used to indicate that only positive values of  $k$  are used and thus it can be applied to either side of the equation (for the convenience of presentation, it is used with,  $\tilde{R}_{k_x, k_y, k'_z}(\omega)$ ), and

$$F_{\text{BL}}(k_x, k_y, k'_z) = A(k)T(k)F(k_x, k_y, k'_z) \quad (16)$$

is a band-limited version of the spatial Fourier transform of the object function, the subscript “BL” means “band-limited”, and the combined transmit and receive transfer function,  $A(k)T(k)$ , of the array transducer can be assumed, for example, to be proportional to the following Blackman window function [24], [62]:

$$W(k) = \begin{cases} 0.42 - 0.5 \cos \frac{\pi k}{k_0} + 0.08 \cos \frac{2\pi k}{k_0}, & 0 \leq k \leq 2k_0 \\ 0, & \text{otherwise} \end{cases} \quad (17)$$

where  $k_0 = 2\pi f_0/c$  and  $f_0$  is the center frequency. The  $-6$  dB bandwidth of  $W(k)$  is about 81% of its center frequency, which is typical for medical ultrasound.

By taking the inverse transformation of (16), an approximation of the object function can be constructed using the definition of the spatial Fourier transform in (14)

$$\begin{aligned} f(\vec{r}) &\approx f_{\text{BL}}(\vec{r}) \approx f_{\text{BL}}^{\text{Part}}(\vec{r}) \\ &= \frac{1}{(2\pi)^3} \int_{-\infty}^{\infty} dk_x \int_{-\infty}^{\infty} dk_y \int_{k \geq \sqrt{k_x^2 + k_y^2}} dk'_z \\ &\quad \times F_{\text{BL}}(k_x, k_y, k'_z) e^{-ik_x x - ik_y y - ik'_z z}, \quad (18) \end{aligned}$$

where the first approximation is due to the finite bandwidth of received signals and the second approximation is due to the requirement that  $k \geq \sqrt{k_x^2 + k_y^2}$  must be satisfied. Thus, only part (indicated by the superscript “Part”) of the spatial Fourier transform of the object function is known [see the area inside the spherical cone in Fig. 2(a) and (b)]. It can be shown from computer simulation (see the following sections) and experiment [56] that these approximations do not significantly affect the quality of constructed images as compared to those obtained with conventional dynamically focused pulse-echo imaging systems.

With (8), the above equation (18) can be written in terms of the other set of independent variables,  $k$ ,  $\zeta$ , and  $\theta$

$$f(\vec{r}) \approx \frac{c^2}{(2\pi)^3} \int_0^{\infty} k^2 dk \int_{-\pi}^{\pi} d\theta \int_0^{\pi/2} \sin \zeta (1 + \cos \zeta) d\zeta \tilde{R}'_{k, \zeta, \theta}(\omega) e^{-ikr \sin \zeta \cos(\phi - \theta) - ik(1 + \cos \zeta)z}, \quad (19)$$

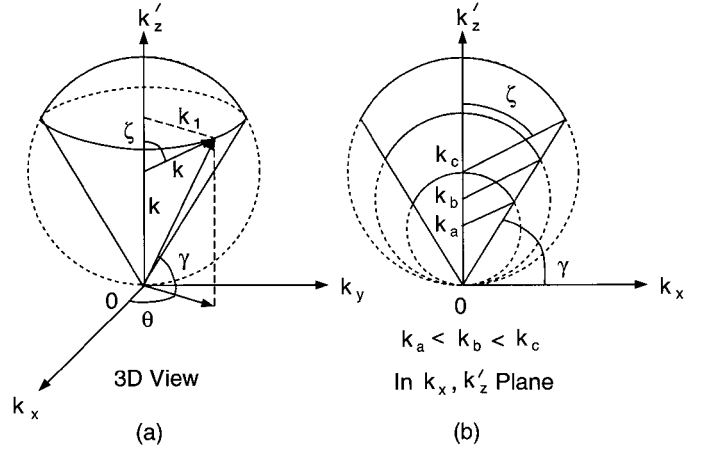


Fig. 2. 3D spatial Fourier-domain coverage of a pulse-echo imaging system where a plane wave pulse (broadband) is used in transmission and limited diffraction beams of different parameters are used in reception. (a) 3D view and (b) view at the  $k_x - k'_z$  plane.  $k_a, k_b$ , and  $k_c$  are three different values of  $k$ .

where  $\tilde{R}'_{k, \zeta, \theta}(\omega) = \tilde{R}_{k_x, k_y, k'_z}(\omega)$ ,

$$dk_x dk_y dk'_z = \left| \frac{\partial(k_x, k_y, k'_z)}{\partial(k, \zeta, \theta)} \right| dk d\zeta d\theta, \quad (20)$$

and where

$$\frac{\partial(k_x, k_y, k'_z)}{\partial(k, \zeta, \theta)} = \begin{vmatrix} \frac{\partial k_x}{\partial k} & \frac{\partial k_x}{\partial \zeta} & \frac{\partial k_x}{\partial \theta} \\ \frac{\partial k_y}{\partial k} & \frac{\partial k_y}{\partial \zeta} & \frac{\partial k_y}{\partial \theta} \\ \frac{\partial k'_z}{\partial k} & \frac{\partial k'_z}{\partial \zeta} & \frac{\partial k'_z}{\partial \theta} \end{vmatrix} = k^2 \sin \zeta (1 + \cos \zeta) \quad (21)$$

is the Jacobian determinant [63]. For a practical array transducer of a finite diameter,  $D$ , the depth of field of the array beams is determined by (2). If one is interested in objects within a given depth of field,  $Z_{\text{max}}$ , the corresponding Axicon angle,  $\zeta_{\text{max}} \leq \pi/2$ , can then be calculated. In this case, the integration over  $\zeta$  in (19) should be from 0 to  $\zeta_{\text{max}}$ . As shown in Fig. 2,  $\zeta_{\text{max}}$  determines the maximum open angle of the spherical cone.

If the object function  $f(\vec{r})$ , is real, which is the case in most applications, the following is true from (14)

$$F(-k_x, -k_y, -k'_z) = F^*(k_x, k_y, k'_z), \quad (22)$$

where the superscript “\*” means complex conjugate. In this case, the spatial Fourier transform of the object function in the lower Fourier space ( $k'_z < 0$ ) is also known.

**2. 2D Image Constructions:** A 2D image in any orientation (including both B-mode and C-mode images) can be readily obtained if a 3D image is constructed with (18) or (19). However, 3D imaging is more complex and generally requires more computation. In the following, formulas that are simplified from (18) and (19) and are suitable for conventional B-mode imaging and a nonconventional C-mode imaging (“nonconventional” means that the imaging is applicable only for an isolated thin-layer object, such as a film, that has a thickness much smaller than a wavelength) will be derived. In B-mode imaging, objects are

assumed to be independent of  $y$  (along the elevation direction), and in C-mode imaging, objects are assumed to be a thin layer located at an axial distance  $z = z_0$  away from the transducer, where  $z_0$  is a constant.

C-mode imaging assumes the object function  $f(\vec{r})$  in (13) represents a thin layer that is in parallel with the surface of a 2D array transducer. This is indicated mathematically as follows:

$$f(\vec{r}) = f^{(1)}(x, y)\delta(z - z_0), \quad (23)$$

where  $\delta$  is the Dirac-Delta function and  $f^{(1)}(x, y)$  is a transverse object function. The received signal is then expressed as follows from (13):

$$\begin{aligned} & R_{k_x, k_y, k'_z}^{(1)}(t) \\ &= \frac{1}{2\pi} \int_{-\infty}^{\infty} \frac{A(k)T(k)H(k)}{c} \left[ \int_S f^{(1)}(x, y) e^{ik_x x + ik_y y} dx dy \right] \\ & \times e^{ik'_z z_0} e^{-i\omega t} dk \\ &= \frac{1}{2\pi} \int_{-\infty}^{\infty} \frac{A(k)T(k)H(k)}{c} F^{(1)}(k_x, k_y) e^{ik'_z z_0} e^{-i\omega t} dk, \end{aligned} \quad (24)$$

where  $S$  is the area of the object and  $F^{(1)}(k_x, k_y)$  is the spatial Fourier transform of  $f^{(1)}(x, y)$ . As with (15) and (16), we then have:

$$\begin{aligned} F_{\text{BL}}^{(1)}(k_x, k_y) &= A(k)T(k)F^{(1)}(k_x, k_y) \\ &= c^2 H(k) \tilde{R}_{k_x, k_y, k'_z}^{(1)}(\omega) e^{-ik'_z z_0}. \end{aligned} \quad (25)$$

From (25), the 2D image of a thin-layer object can be constructed approximately with the 2D inverse spatial Fourier transform as follows:

$$\begin{aligned} f^{(1)}(x, y) &\approx f_{\text{BL}}^{(1)}(x, y) \\ &= \frac{1}{(2\pi)^2} \int_{\sqrt{k_x^2 + k_y^2} \leq k} \int F_{\text{BL}}^{(1)}(k_x, k_y) e^{-ik_x x - ik_y y} dk_x dk_y. \end{aligned} \quad (26)$$

Equation (26) can be evaluated by either fixing the wave number (monochromatic),  $k = k_0 = 2\pi f_0/c$ , where  $f_0$  is the center temporal frequency of the pulse-echo system, or fixing the Axicon angle,  $\zeta = \zeta_{\text{max}}$ , and then changing  $k$  (broadband). For the monochromatic case,  $k = k_0$ , we have:

$$\begin{aligned} f^{(1)}(x, y) &\approx \frac{c^2}{(2\pi)^2} \int_{\sqrt{k_x^2 + k_y^2} \leq k_0} \int \left[ \tilde{R}_{k_x, k_y, k'_z}^{(1)}(\omega_0) e^{-ik'_z z_0} \right] \\ & \times e^{-ik_x x - ik_y y} dk_x dk_y, \end{aligned} \quad (27)$$

where  $\omega_0 = k_0 c$ . If  $\zeta = \zeta_{\text{max}}$  is fixed, from (8), we obtain

$$\begin{aligned} f^{(1)}(x, y) &\approx \frac{c^2 \sin^2 \zeta_{\text{max}}}{(2\pi)^2} \\ & \cdot \int_0^{\infty} k dk \int_{-\pi}^{\pi} d\theta \left[ \tilde{R}_{k, \zeta_{\text{max}}, \theta}^{(1)'}(\omega) e^{-ik(1 + \cos \zeta_{\text{max}})z_0} \right] \\ & \times e^{-ikr \sin \zeta_{\text{max}} \cos(\phi - \theta)}, \end{aligned} \quad (28)$$

where  $\tilde{R}_{k, \zeta, \theta}^{(1)'}(\omega) = \tilde{R}_{k_x, k_y, k'_z}^{(1)}(\omega)$ . Notice that in the monochromatic case, if the aperture is finite, there may be many points in the space where the transmit beam is zero in amplitude due to the interference of edge waves. However, the influence of edge wave can be reduced dramatically with an aperture weighting such as the cosine weighting at the expense of reduced effective aperture size.

To construct B-mode images, it is assumed that the object function  $f(\vec{r})$  is given by  $f(\vec{r}) = f^{(2)}(x, z)$ . That is, the object is uniform along the  $y$  direction. In this case, it is not necessary to weight array transducers in the  $y$  direction, and thus a 1D array transducer instead of a 2D array can be used.

From (5), broadband layered array beams can be derived by setting the free parameter,  $k_y$ , to zero [29]–[31]

$$\Phi_{\text{Layer}}(x, z, t) = \frac{1}{2\pi} \int_{-\infty}^{\infty} T(k)H(k) e^{ik_x x + ik_z z} e^{-i\omega t} dk, \quad (29)$$

where the subscript ‘‘Layer’’ represents ‘‘layered array beams,’’  $k'_z = k + k_z$ , and where

$$\begin{cases} k_x = k \sin \zeta \\ k_z = \sqrt{k^2 - k_x^2} = k \cos \zeta \geq 0 \end{cases} \quad (30)$$

is a special case of (8) with  $\theta \equiv 0$ .

From (13), the resulting received signal is as follows:

$$\begin{aligned} & R_{k_x, k'_z}^{(2)}(t) \\ &= \frac{1}{2\pi} \int_{-\infty}^{\infty} \frac{A(k)T(k)H(k)}{c} \left[ \int_S f^{(2)}(x, z) e^{ik_x x + ik'_z z} dx dz \right] \\ & \times e^{-i\omega t} dk \\ &= \frac{1}{2\pi} \int_{-\infty}^{\infty} \frac{A(k)T(k)H(k)}{c} F^{(2)}(k_x, k'_z) e^{-i\omega t} dk, \end{aligned} \quad (31)$$

where  $F^{(2)}(k_x, k'_z)$  is the spatial Fourier transform of  $f^{(2)}(x, z)$  and ‘‘S’’ is an area in the  $x - z$  plane. [Because  $k'_z \geq k$  ( $k \geq 0$ ), the spatial Fourier transform of  $f^{(2)}(x, z)$  is known only in the area shown in Fig. 2(b).]

If  $f(\vec{r})$  is also a function of  $y$ , the  $f^{(2)}(x, z)$  in (31) is an effective 2D object function that is given by:

$$f^{(2)}(x, z) = \int_{-\infty}^{\infty} f(\vec{r}) dy. \quad (32)$$

In most B-scan systems, beams are focused with a lens in the elevation direction ( $y$  direction), the slice thickness is quite small at focus and the effective 2D object function in (32) can be written as follows:

$$f^{(2)}(x, z) \approx f(x, y_0, z)d_y, \quad (33)$$

where  $y_0$  is the center plane of the slice defined by the elevation focus and  $d_y$  is the slice thickness (notice that the focusing in the  $y$  direction will not affect the layered array beams in the  $x$  direction [29] and Fig. 5 in [20]).

From (31), it follows:

$$F_{\text{BL}}^{(2)}(k_x, k'_z) = A(k)T(k)F^{(2)}(k_x, k'_z) = c^2 H(k)\tilde{R}_{k_x, k'_z}^{(2)}(\omega), \quad (34)$$

where  $\tilde{R}_{k_x, k'_z}^{(2)}(\omega)$  is the temporal Fourier transform of  $R_{k_x, k'_z}^{(2)}(t)$ . The effective object function can be constructed approximately by inverse spatial Fourier transformation of  $F_{\text{BL}}^{(2)}(k_x, k'_z)$  in (34):

$$\begin{aligned} f^{(2)}(x, z) &\approx f_{\text{BL}}^{(2)}(x, z) \approx f_{\text{BL}}^{(2)\text{Part}}(x, z) \\ &= \frac{1}{(2\pi)^2} \int_{-\infty}^{\infty} dk_x \int_{k \geq |k_x|} dk'_z F_{\text{BL}}^{(2)}(k_x, k'_z) e^{-ik_x x - ik'_z z}. \end{aligned} \quad (35)$$

Using (30), (35) can be written as:

$$\begin{aligned} f^{(2)}(x, z) &\approx \frac{c^2}{(2\pi)^2} \int_0^{\infty} k dk \int_0^{\pi/2} (1 + \cos \zeta) d\zeta \\ &\times \tilde{R}_{k, \zeta}^{(2)'}(\omega) e^{-ikx \sin \zeta - ik(1 + \cos \zeta)z}. \end{aligned} \quad (36)$$

### III. COMPUTER SIMULATIONS

In the following, simulations of both 2D C-mode and 3D pulse-echo imaging are described. 2D B-mode imaging is simulated with parameters corresponding to experiments [56]. In fact, 2D B-mode imaging is a special case of 3D [compare (19) and (36)] but using a conventional linear array and simpler electronics. In the following simulations, Rayleigh-Sommerfeld diffraction formula [24], [64] is used.

In the simulations, we assume that the transducer is a circular 2D array (Fig. 1). The diameter of the transducer,  $D$ , is 50 mm. The transducer is broadband and its center frequency is 2.5 MHz. The bandwidth of the transducer is about 81% of the center frequency [assume that the combined transmit and receive transfer function is proportional to the Blackman window function given in (17)] [24]. The background medium is assumed to be water that has a speed of sound of 1500 m/s giving a wavelength of 0.6 mm at the center frequency. The objects are assumed to be composed of point scatterers. The inter-element distance of the array transducer is assumed to be 0.3 mm in both  $x$  and  $y$  directions. In transmission, all the array elements are connected electronically to transmit a plane

wave pulse (broadband). Echoes from objects (Fig. 1) are received with the same array that is weighted to produce limited diffraction receptions. By choosing a pair of spatial weighting frequencies,  $k_x$  and  $k_y$ , one obtains the spatial Fourier transform of the object function evaluated at these frequencies [see (13) for 3D and (24) for 2D] (this is similar to the frequency and phase encoding in MRI (magnetic resonance imaging) [65], [66]). Given  $k_x$  and  $k_y$ ,  $k'_z$  is determined by  $k$  that is related to the temporal frequency by  $k = 2\pi f/c$ .

To use the FFTs and IFFTs directly,  $k_x$  and  $k_y$  are chosen at rectangular grids. The temporal spectra [(15) and (25)] of the received signals are calculated by the FFTs for each pair of  $k_x$  and  $k_y$ . Using the nearest-neighbor interpolation [67], the Fourier transform of the object functions at  $k'_z$  can be determined with the formula

$$k'_z = k + k_z = k + \sqrt{k^2 - k_x^2 - k_y^2} \quad (37)$$

for 3D image constructions. For 2D C-mode imaging, the following formula (27) (monochromatic or fixed frequency)

$$k'_z = k_0 + \sqrt{k_0^2 - k_x^2 - k_y^2} \quad (38)$$

or (28) (broadband or fixed Axicon angle)

$$k'_z = k(1 + \cos \zeta) \quad (39)$$

is used in the interpolation. In the broadband 2D C-mode imaging, a short time gate (a Blackman window function having a width of 2.4  $\mu\text{s}$ ) is applied to the received signals to select a layer at  $z = z_0$ .

### IV. RESULTS

Results of both 2D C-mode and 3D pulse-echo imaging are given in the following. These results indicate that the approximations (18) due to a finite temporal bandwidth and limited spatial Fourier-domain coverage that are typical in medical ultrasonic imaging do not significantly affect the quality of constructed images in terms of spatial resolutions, sidelobes, and contrast.

For 2D C-mode imaging, single layer objects used for the constructions are shown in Figs. 3(a) and (b). These objects are located at  $z = z_0$  and are composed of either a single point scatterer [Fig. 3(a)] on the axis of the transducer or 24 point scatterers forming a stacked letter ‘‘L’’ [Fig. 3(b)]. The dimensions of the objects are shown in Fig. 3. Images constructed with (28) (broadband—with a fixed  $\zeta$ ) at several axial distances are shown in Fig. 4. With the parameters given in Fig. 4, the depth of field of the limited diffraction array beams (5) or X waves (1) is about 216 mm (2). At the boundary of the depth of field, it is seen that images start to degrade (see images at  $z_0 = 200$  mm in Fig. 4).

To see the sidelobes of the constructed images, line plots along the  $x$  axis of the single point scatterer (PSF or point

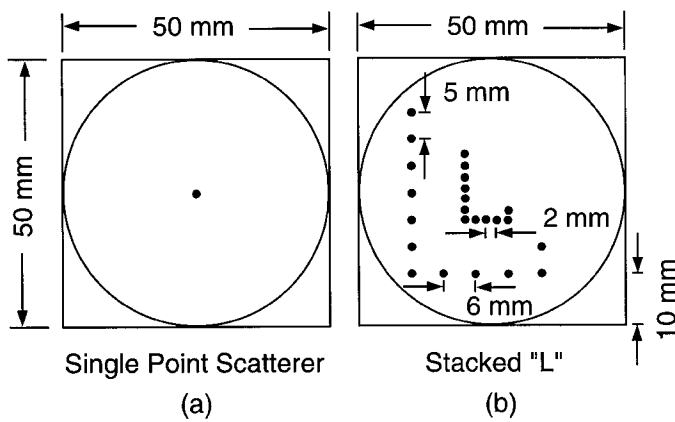


Fig. 3. Single-layer objects (lay in a plane perpendicular to the beam axis) for 2D C-mode imaging. (a) Single point scatterer. (b) Stacked letters "L" consisting of multiple point scatterers.

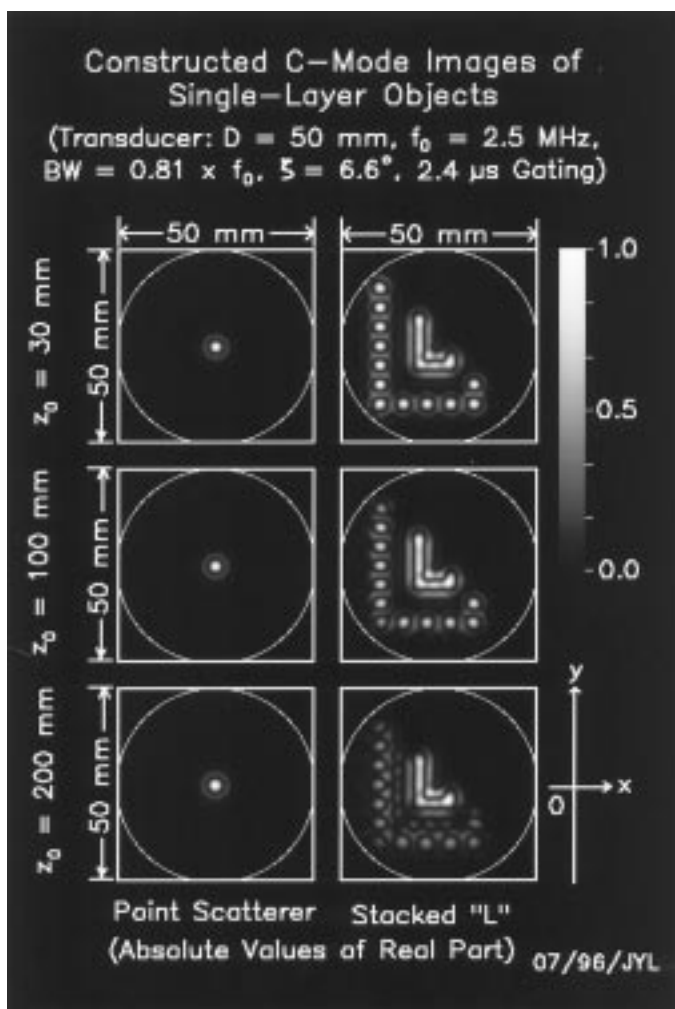


Fig. 4. Constructed 2D C-mode images of the single-layer objects. Panels in the top, middle, and bottom rows correspond to images constructed at the axial distances,  $z_0 = 30, 100,$  and  $200$  mm, respectively. Panels on the left and right columns are constructed images of the single point scatterer and stacked "L" corresponding to Figs. 3(a) and (b), respectively. Absolute values of the real part of the constructed images are shown. Transducer parameters are given on the top of the images. The circle surrounding each image indicates the area of transducer aperture.

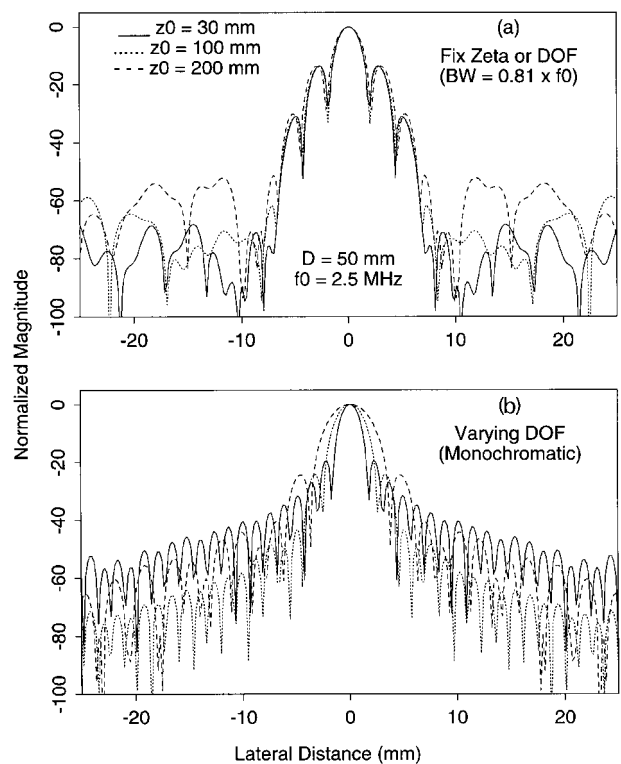


Fig. 5. (a) Line plots of the constructed 2D C-mode images of the point scatterer in the left column of Fig. 4 along the  $x$  axis at three axial distances:  $z = 30$  (solid lines),  $100$  (dotted lines), and  $200$  mm (dashed lines). These plots are obtained with a fixed Axicon angle,  $\zeta = 6.6^\circ$ . (b) Line plots of constructed 2D C-mode images (not shown) of the point scatterer with a fixed temporal frequency ( $2.5$  MHz) but varying  $\zeta$  within  $6.6^\circ$ . The plots have the same format as those in Panel (a). The unit of vertical axes is dB

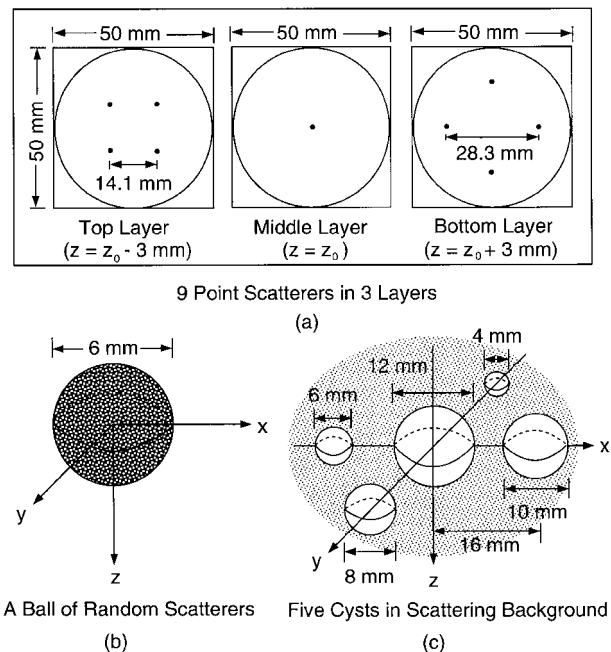


Fig. 6. 3D objects for 3D image constructions. (a) A three-layer object consisting of 9 point scatterers. The separation between layers is 3 mm. (b) A 6 mm diameter sphere of random point scatterers. (c) 5 cystic spheres embedded in a background of random scatterers.

spread function) are shown in Fig. 5(a). For comparison, line plots of images of the same point scatterer constructed with (27) for a fixed frequency,  $k_0 = 2\pi f_0$ , where  $f_0 = 2.5$  MHz (monochromatic), are shown in Fig. 5(b). In this case, the lateral resolution of images decreases with the increase of depth (no longer limited diffraction). This is due to the change of the Axicon angle,  $\zeta$ , as  $k_x$  and  $k_y$  change.

Three 3D objects are used for 3D image constructions (Fig. 6). The first is an object consisting of 9 point scatterers in 3 layers separated by 3 mm between the layers. The geometry of each layer is shown in Fig. 6(a). The second is a sphere of radius of 3 mm [Fig. 6(b)]. It consists of numerous randomly positioned point scatterers and its center is on the axis of the transducer. The last object consists of 5 cystic spheres of different diameters embedded in random scattering background [Fig. 6(c)].

Images of the 3-layer object constructed with (18) or (19) are shown in Fig. 7. Both 3D and 2D views are presented. It is seen that the lateral resolution of the constructed images degrades with depth. This is due to the fact that smaller Axicon angles have to be used to increase the depth of field (2) of limited diffraction beams [(1) and (5)] at larger depths. Line plots along the  $x$  and  $z$  axes are shown in Figs. 8(a) and (b), respectively. From both Fig. 7 and Fig. 8(b), it is seen that the edge waves of the unshaded transmit plane wave produce artifacts behind the main images near the axis of the transducer. The edge waves can be reduced by a proper aperture weighting of the transmission aperture and then unshade the constructed images to recover from the weighting effects (assume that there are no zeroes in the weighting functions).

Constructed 3D images of the sphere of random scatterers are shown in Fig. 9. Similar to Fig. 7, lateral resolution of the images in Fig. 9 degrades with depth. The formula used for the constructions is the same as that for Fig. 7. Line plots of the constructed images of the sphere along the  $x$  and  $z$  axes through the center of the sphere are shown in Figs. 10(a) and (b), respectively.

Images of 5 cystic spheres constructed with (18) or (19) are shown in Fig. 11. The constructed images are displayed at 3 perpendicular planes ( $x$ ,  $y$ , and  $z$ ) intersected at the center of the center sphere. From Fig. 11, it is seen that images constructed with the new method also have a high contrast (notice that images in this figure is log compressed).

## V. A SUGGESTED IMAGING SYSTEM

The theory of the new imaging method developed in the previous sections can be implemented with a suggested system described in the following for 3D high frame rate imaging [(18) or (19)]. For 2D B-mode imaging [(35) or (36)], the system can be scaled down by one dimension (setting the free parameter,  $k_y$ , to zero), which greatly simplifies both the transducer and electronics required by the system (replacing the 3D IFFT with 2D and using a 1D array transducer).

To illuminate objects such as biological soft tissues within a finite aperture and a depth of interest (e.g., 200 mm in medical ultrasound), a uniform plane wave pulse (broadband) is transmitted by a 2D array transducer with all of its elements connected together electronically (Fig. 12). The plane wave may be weighted near the edges (heavy weighting may reduce the effective transducer aperture and thus reduce the effective viewing area) to reduce edge waves. After images are constructed, the weighting effects can be compensated with the inversion of the transmit weighting function.

Waves scattered from the objects are received with the same array transducer that is used in transmission. Signal from each element is connected to a T/R (transmit/receive) switch and then pre-amplified and compensated for attenuation with a TGC (time-gain control) chip. The received echo signals are gated so that a slice of tissue (along the  $z$  direction) of thickness,  $d_z$ , can be selected. The gated signals are then weighted with either grid array beams (5) for 3D or layered array beams (29) for 2D B-mode imaging to produce A-lines. The weightings are simple cosine and sine functions and can be approximated with piecewise steps (the step size is determined by the inter-element distance of the array transducers). To use the FFT and IFFT algorithms directly, the free parameters of the limited diffraction beams,  $k_x$  and  $k_y$ , are chosen so that they fall exactly at the rectangular grids of the spatial Fourier domain (Fig. 2) of the objects. The sampling intervals of  $k_x$  and  $k_y$  are determined by the dimensions,  $d_x$  and  $d_y$ , of constructed images in the  $x$  and  $y$  directions, respectively (i.e.,  $\Delta k_x \leq 2\pi/d_x$  and  $\Delta k_y \leq 2\pi/d_y$ ). The number of samples,  $N_x$  and  $N_y$ , in these directions are determined by the spacing of the constructed images in the corresponding directions. The acquired A-lines are digitized with A/D converters at a rate that satisfies the Nyquist sampling theorem [62] and their temporal spectra can be obtained with DSP chips or ASIC (application specific integrated circuits). The Fourier transform of objects at the equal-distance intervals along the  $k'_z$  direction are obtained from the discrete temporal spectra of the A-lines with the nearest-neighbor interpolation using the formula:

$$k = \frac{k_z'^2 + k_x^2 + k_y^2}{2k_z'}, \quad k_z' \geq \sqrt{k_x^2 + k_y^2}. \quad (40)$$

At points where (40) is not satisfied, the Fourier space is simply filled with zeroes. Similar to  $k_x$  and  $k_y$ , the sampling interval along  $k'_z$  [(18) and (35)] is determined by the inversion of the thickness of constructed images (i.e.,  $\Delta k'_z \leq 2\pi/d_z$ ), and the number of samples in the  $z$  direction,  $N_z$ , is determined by the step size of the constructed images in this direction. Because object functions are assumed to be real, their spatial Fourier transform at  $k'_z < 0$  (lower part of Fig. 2) can be determined from that at  $k'_z \geq 0$  (22). The formula (40) can be implemented with a lookup table stored in a ROM (read-only memory) or an

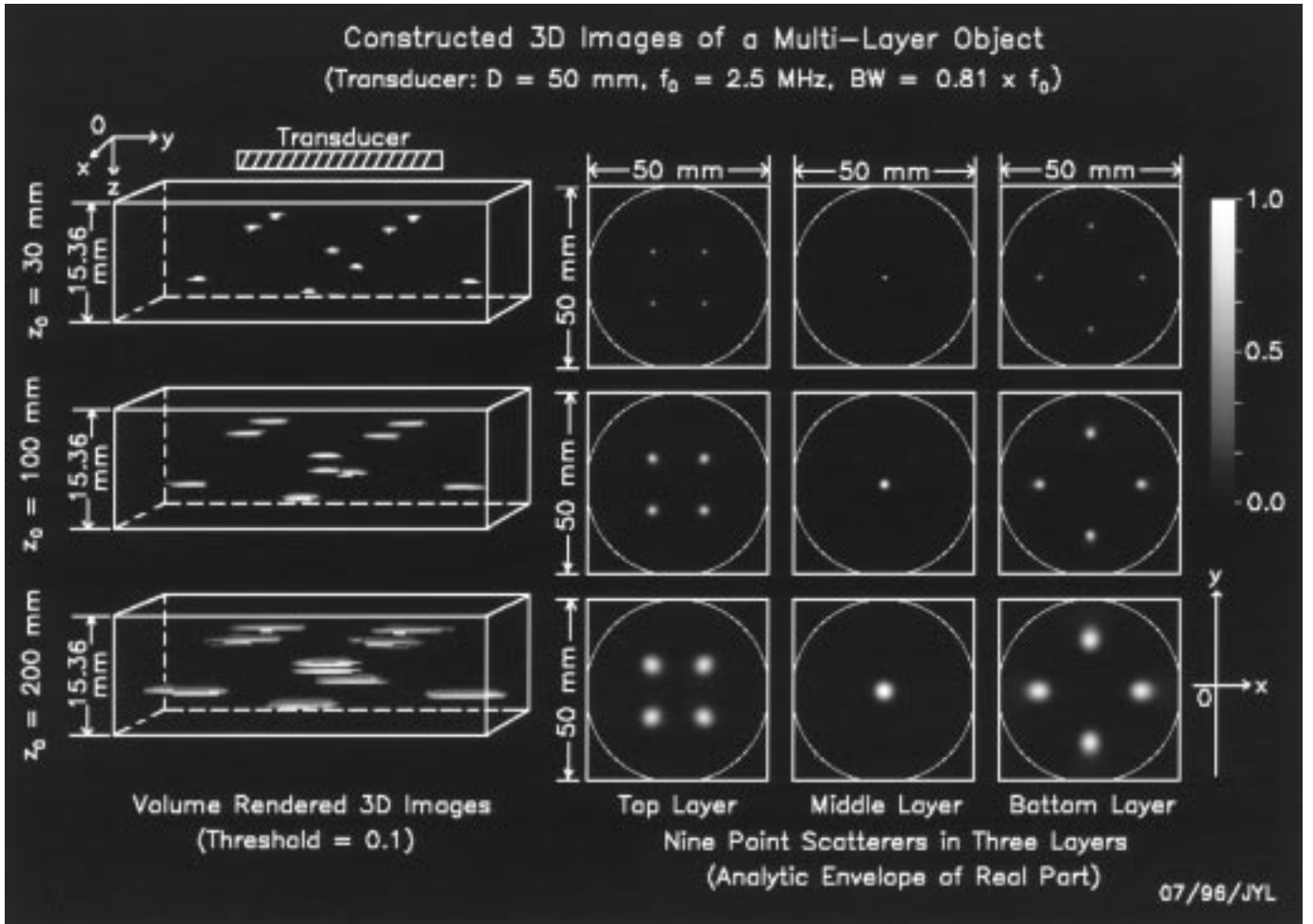


Fig. 7. Constructed 3D images of the three-layer object in Fig. 6(a). Panels in the left column are 3D volume rendered images with a threshold of 0.1 (maximum is 1.0). Images are rendered with the commercial software package ANALYZE<sup>®</sup> (Mayo Clinic, Rochester, MN.). The size of constructed volumes is  $50 \times 50 \times 15.36$  mm<sup>3</sup>. Transducer is assumed to be on top of the volumes. The three layers of the constructed images are displayed separately on the right hand side of the volume rendered images. These layers correspond to those in Fig. 6(a). Panels in the top, middle, and bottom rows correspond to the axial distances of the center of the object at  $z = 30, 100,$  and  $200$  mm, respectively.

FPGA (field programmable array), to generate necessary  $k$  values for the interpolations. After obtaining the spatial Fourier transform of the object functions at all rectangular grids of  $k_x, k_y,$  and  $k'_z,$  images are constructed by DSP chips or ASIC that perform a 3D IFFT.

The beamforming method above is completely different from the one (dynamic focusing) currently used in all 2D B-mode and 3D imaging [44]–[46]. The advantages of the FFT-based beamformer are low cost and high speed. Because only one transmission is required to construct images, the theoretical frame rate can be as high as 3750 frames/second for biological soft tissues at a 200 mm depth. In practice, the frame rate will be limited by the speed of the electronics, DSP or ASIC chips, and the speed to process the large amount of 3D data for display (such as volume rendering and surface extraction, etc.), as well as the monitor refresh rate. The potential high frame rate imaging will be less subject to motion artifacts of fast moving objects such as the heart leaflet and will make 3D flow vector imaging or angiography possible [42].

## VI. DISCUSSION

### A. Resolutions

From Figs. 5 and 8, it is seen that the resolutions of images constructed with the new method are high (the theoretical diffraction-limited  $-6$  dB lateral beamwidth of a focused piston beam at focus is given by  $0.71\lambda z/(D/2)$  (see p. 425 of [4]), which is  $5.68\lambda$  for  $D = 50$  mm and  $z = 200$  mm). The  $-6$  dB resolutions of both 2D C-mode and 3D imaging at three axial distances from the transducer are listed in terms of the wavelength ( $\lambda = 0.6$  mm) in Table I. With a fixed Axicon angle,  $\zeta = 6.6^\circ$ , the depth of field of the limited diffraction beams given by (2) or (5) is also fixed. This allows a nearly constant lateral resolution over a large depth of interest in 2D C-mode imaging [Figs. 4 and 5(a)]. If the temporal frequency is fixed at  $f_0 = 2.5$  MHz (monochromatic) but the Axicon angle is allowed to vary,  $0 \leq \zeta \leq \zeta_{\max} = 6.6^\circ$ , the lateral resolution of 2D C-mode images changes significantly with the axial distance [Fig. 5(b)]. Notice that the constraint,

TABLE I

−6 dB LATERAL AND AXIAL BEAM-WIDTHS (RESOLUTION) OF CONSTRUCTED IMAGES OF A POINT TARGET (POINT SPREAD FUNCTION) IN TERMS OF WAVELENGTH,  $\lambda$ . FOR COMPARISON, THE THEORETICAL DIFFRACTION-LIMITED −6 dB LATERAL BEAM-WIDTHS OF A FOCUSED PISTON TRANSDUCER (DIAMETER  $D=50$  MM) AT FOCUS ARE ALSO LISTED. AS THE AXICON ANGLE ( $\zeta < \pi/2$ ) INCREASES, ONE CAN EXPECT THAT THE LATERAL RESOLUTION OF CONSTRUCTED IMAGES WILL APPROACH TO THE DIFFRACTION LIMIT [56].

		2D C-Mode Imaging			
		Fixed $\zeta$ or depth of field	Monochromatic ( $f_0 = 2.5$ MHz)	3D imaging	Focused piston (diffraction limit)
Lateral resolution	$z = 30$ mm	$4.58\lambda$	$3.75\lambda$	$1.25\lambda$	$0.85\lambda$
	$z = 100$ mm	$4.58\lambda$	$6.25\lambda$	$3.33\lambda$	$2.84\lambda$
	$z = 200$ mm	$5.42\lambda$	$8.75\lambda$	$6.67\lambda$	$5.68\lambda$
Axial resolution	$z = 30$ mm	N/A	N/A	$\leq 0.833\lambda$	
	$z = 100$ mm	N/A	N/A	$\leq 0.833\lambda$	
	$z = 200$ mm	N/A	N/A	$\leq 0.833\lambda$	

$\zeta_{\max} = 6.6^\circ$ , is used to keep the number of samples constant in the Fourier space (assume that the distance between samples is the same) for both the monochromatic (varying  $\zeta$ ) and broadband (fixed  $\zeta$ ) 2D C-mode imaging.

In 3D image constructions (Figs. 7 to 11), the maximum Axicon angle,  $\zeta_{\max}$ , is determined by the formula:

$$\zeta_{\max} = \tan^{-1} \left( 0.926 \frac{D}{2z_0} \right), \quad (41)$$

where  $z_0$  is the axial distance between the transducer and the center of objects, and the constant, 0.926, is used to allow the actual depth of field to be a little larger than  $z_0$ . (Actually, from the experiment [56] one sees that a constant that is much larger than 0.926 can be used to enhance the lateral resolution without degrading image quality. With this technique, the lateral resolution of the 3D images may be more close to the diffraction limit given above and listed in Table I. However, a larger  $\zeta$  requires a greater amount of computation in 3D simulation.) For  $z_0 = 30, 100,$  and  $200$  mm,  $\zeta_{\max} = 37.6^\circ, 13.0^\circ,$  and  $6.60^\circ$ , respectively. From (8), we see that a larger  $\zeta_{\max}$  will allow larger  $k_x$  and  $k_y$  for a given transducer bandwidth. The lateral resolution enhancement with the decrease of the axial distance,  $z_0$  (or the increase of the maximum Axicon angle,  $\zeta_{\max}$ ), is clearly seen from Figs. 7 and 8 and Table I.

*B. Sidelobes*

Sidelobes of constructed 2D C-mode and 3D images are shown in Figs. 5, 8, and 10. With the new method, sidelobes of constructed images decrease with the sampling intervals,  $\Delta k_x, \Delta k_y,$  and  $\Delta k'_z$ , in the spatial Fourier domain. Sidelobe levels for 2D C-mode imaging shown in Fig. 5 are achieved with  $\Delta k_x = \Delta k_y = 2\pi/100 \text{ mm}^{-1}$ . For 3D imaging,  $\Delta k_x = \Delta k_y = 2\pi/60 \text{ mm}^{-1}$  and  $\Delta k'_z = 2\pi/15.36 \text{ mm}^{-1}$ . A recent study by the author shows that sidelobes can also be greatly reduced (almost doubled in dB scale) with a cosine weighting at the receiving aperture. However, a heavier aperture weighting is at the expense of the lateral resolution and lateral field of view of constructed images.

*C. Depth of Field*

Depth of field (2) of limited diffraction array beams are the same as that of X waves for a given aperture size and Axicon angle [30], [31]. In 3D imaging, the minimum depth of field of the beams can be adjusted to the depth of interest to maximize the lateral resolution (this is the case for Figs. 7 to 11). The depth of field for the plane wave pulse is usually much larger than that of limited diffraction beams and thus needs not to be considered. If one wishes to fix the minimum depth of field, or the maximum Axicon angle, the volume of the spherical cone [Fig. 2(a)] in the spatial Fourier domain will remain the same. This will result in a nearly uniform lateral resolution for constructed images at all axial depths (see Fig. 4 and Table I).

*D. Edge Waves*

The influence of edge waves of unshaded plane wave transmission is clearly seen near the axis of the transducer (Figs. 7 to 10). The influence can be reduced dramatically if the transmitting aperture is weighted properly (see Fig. 7 of [24]). After images are constructed, the influence of the weighting can be compensated as was discussed in the previous sections.

*E. Frame Rate*

The new method has a potential for high frame rate imaging (up to about 3750 frames/second for biological soft tissues at a 200 mm depth). This is possible because multiple transmissions of ultrasound beams are not necessary to construct images. Multiple transmissions reduce image frame rate due to the finite speed of sound of objects such as biological soft tissues [45], [46]. The high frame rate will reduce artifacts in imaging of fast moving objects such as the heart and is particularly useful for diagnosing congenital diseases of fetus hearts.

### F. 3D Blood Flow Vector Imaging

With the high frame rate capability of the new method, two consecutive volumes of 3D RF (radio frequency) data or images can be acquired and stored for speckle tracking analysis [42]. This enables 3D flow vector imaging, which may overcome many problems associated with conventional Doppler blood flow techniques [42].

### G. Underwater Acoustic Imaging

In underwater acoustic imaging, objects are usually further away from transducer as compared to those in medical ultrasound [43]. Given a finite speed of sound of water, it is difficult to construct images at a high frame rate with conventional imaging methods. The new method proposed in this paper offers an opportunity for high quality underwater acoustic imaging at a high frame rate.

### H. 2D Transducer Designs

For 2D C-mode or 3D imaging, a 2D array transducer is required for the new method. The inter-element distances of the transducer along the  $x$  and  $y$  axes are determined by the highest spatial frequencies in  $k_x$  and  $k_y$ , respectively [62]. In current medical ultrasonic imaging, lateral resolution is usually much lower than axial resolution, and therefore, maximum  $k_x$  and  $k_y$  are much smaller than  $k_{\max}$ . For example, if  $\zeta \leq \zeta_{\max} = 6.6^\circ$ , from (8) we obtain  $\sqrt{k_x^2 + k_y^2} \leq k_{\max} \sin \zeta_{\max} = 0.115k_{\max}$ , where  $k_{\max}$  is determined by the highest temporal frequency. This means that the inter-element distance of the 2D array can be much larger than that of a fully sampled 2D array where the inter-element spacing is usually less or equal to  $\lambda_{\min}/2 = \pi/k_{\max}$  [33] for electronic steering. The large inter-element distance reduces dramatically the number of elements which is inversely proportional to the square of the inter-element distance. High grating lobes resulted from the large inter-element distance can be eliminated with the sub-dicing technique used in commercial array transducers.

### I. 2D B-Mode Imaging

The new method has also been used for 2D B-mode imaging [56]. In this case a commercially available 1D array transducer is used to replace the 2D array in Figs. 1 and 12. The 1D array may focus in the  $y$  direction with a physical lens to obtain a thin slice thickness near the focus [20], [29]. The echo signals are weighted in the  $x$  direction to produce broadband limited diffraction layered array beams (29) [29]–[31]. Equation (35) or (36) is used to construct 2D B-mode images at a high frame rate. Compared to the 3D imaging system in Fig. 12, a 2D B-mode system is greatly simplified since all the electronics are scaled down by one dimension. The discussion above for the design of 2D array transducer applies also to that of 1D arrays for 2D B-mode imaging.

### J. Beam Steering

Although steering is not necessary to construct either 2D or 3D images using the new method, beams of the imaging system in Fig. 12 can be steered electronically to increase image field of view. In this case, the inter-element distance of the array transducer in the scan direction must be smaller than or equal to  $\lambda_{\min}/2$  to eliminate grating lobes [33]. In the elevation direction, the inter-element distance can still be large. Linear time delays required for the steering can be added in either the time domain or temporal frequency domain. Apparently, electronic steering increases the system complexity.

A recent computer simulation by the author indicates that a field of view which is much larger than the transmission aperture can be obtained without beam steering if limited diffraction array beams are used in both transmission and reception (see the following subsection), even if both the transmission and reception apertures are weighted with a cosine function to reduce sidelobes. This is because the transmission and reception beams are always in the same directions, which is different from the plane wave transmission where objects lay outside of the transmission aperture are not illuminated and thus no images can be constructed for these objects.

### K. Increasing Spatial Fourier-Domain Coverage

As shown in Fig. 2, only part of spatial Fourier domain is acquired by the measured backscattered signals. Several methods can be used to increase the Fourier-domain acquisition and thereby increase image resolution. If the imaging system in Fig. 1 is rotated around the object, the spherical cone in Fig. 2 is rotated accordingly. Such rotations increase the Fourier-domain acquisition, but complicate the imaging system, reduce the system accessibility to the human body, and reduce image frame rate.

Without rotating the imaging system, a more complete spatial Fourier-domain coverage can also be obtained by both transmitting and receiving limited diffraction beams. If in (12) and (13) the plane wave pulse produced during the transmission mode is replaced with limited diffraction array beams, the received signal is as follows:

$$\begin{aligned} & R_{k'_x, k'_y, k'_z}^{(\text{PEa})}(t) \\ &= \frac{1}{2\pi} \int_{-\infty}^{\infty} \frac{T^2(k)H(k)}{c} \left[ \int_V f(\vec{r}) e^{ik'_x x + ik'_y y + ik'_z z} d\vec{r} \right] e^{-i\omega t} dk \\ &= \frac{1}{2\pi} \int_{-\infty}^{\infty} \frac{T^2(k)H(k)}{c} F^{(\text{PEa})}(k'_x, k'_y, k'_z) e^{-i\omega t} dk, \end{aligned} \quad (42)$$

where the superscript “(PEa)” means “pulse-echo with array beams,”  $k'_x = 2k_x$ ,  $k'_y = 2k_y$ , and  $k'_z = 2k_z$ . As with (19), using (8), a 3D image construction is then obtained

according to the following formula:

$$f(\vec{r}) \approx \frac{8c^2}{(2\pi)^3} \int_0^\infty k^2 dk \int_{-\pi}^\pi d\theta \int_0^{\pi/2} \sin \zeta d\zeta \tilde{R}_{k,\zeta,\theta}^{(\text{PEa})'}(\omega) e^{-i2kr \sin \zeta \cos(\phi-\theta) - i2kz \cos \zeta}, \quad (43)$$

where  $\tilde{R}_{k,\zeta,\theta}^{(\text{PEa})'}(\omega) = \tilde{R}_{k'_x,k'_y,k'_z}^{(\text{PEa})}(\omega)$  is the temporal Fourier transform of (42), and “ $\approx$ ” sign means approximation due to the finite temporal bandwidth of practical systems. The spatial Fourier coverage is shown in Fig. 13 that is the upper half sphere when  $\zeta_{\max} = \pi/2$ . If object functions are real, the lower half of the Fourier space is also known (22). For 2D B-mode imaging, (42) and (43) can be reduced to 2D in a way similar to that discussed above for plane wave transmission [(29) to (36)]. (Notice that in 2D cases, Soumekh [69] has developed a similar relationship for phased-array imaging. However, in his method, beam steering is required to construct images). Because multiple transmissions are required to implement (42) and (43), the frame rate drops significantly for 3D imaging. However, for 2D B-mode imaging, the same frame rate as that of current commercial B-scanners can be achieved with simpler electronics and beamformer. Because of the increased coverage of the spatial Fourier domain, lateral resolution of constructed images is increased. (A computer simulation of a point spread function of a 2D B-mode imaging system and an object consists of several point scatterers has been performed recently by the author with the new method and a great enhancement on lateral resolution has been observed.)

If objects themselves emit waves (objects are radiation sources) and limited diffraction array beams are used in reception, a formula for the received signal that is similar to (13) is given as follows:

$$\begin{aligned} & R_{k_x,k_y,k_z}^{(\text{One-way})}(t) \\ &= \frac{1}{2\pi} \int_{-\infty}^\infty T(k)H(k) \left[ \int_V f(\vec{r}) e^{ik_x x + ik_y y + ik_z z} d\vec{r} \right] e^{-i\omega t} dk \\ &= \frac{1}{2\pi} \int_{-\infty}^\infty T(k)H(k) F^{(\text{One-way})}(k_x, k_y, k_z) e^{-i\omega t} dk, \end{aligned} \quad (44)$$

where the superscript “One-way” means “receive-only.” 3D images can be constructed approximately (approximation is due to a finite temporal bandwidth) with the following formula:

$$f(\vec{r}) \approx \frac{c}{(2\pi)^3} \int_0^\infty k^2 dk \int_{-\pi}^\pi d\theta \int_0^{\pi/2} \sin \zeta d\zeta \tilde{R}_{k,\zeta,\theta}^{(\text{One-way})'}(\omega) e^{-ikr \sin \zeta \cos(\phi-\theta) - ikz \cos \zeta}, \quad (45)$$

where  $\tilde{R}_{k,\zeta,\theta}^{(\text{One-way})'}(\omega) = \tilde{R}_{k_x,k_y,k_z}^{(\text{One-way})}(\omega)$  is the temporal Fourier transform of (44). The spatial Fourier coverage

for (45) is still the upper half sphere shown in Fig. 13 if  $\zeta_{\max} = \pi/2$ . However, the radius of the sphere is half of that given by (43). For real object functions, the lower half of the sphere is also known (22). This method may have applications in remote sensing of radiating objects such as those in space.

Finally, if the plane wave pulse in (10) is on the opposite side of limited diffraction beam receiver (transmission mode), the received signals are still given by (13) except that the sign of  $k$  in the spatial Fourier transform of the object functions is negative (i.e.,  $k'_z = k_z - k$ ). This moves the spherical cone in Fig. 2 down by  $2k$  along the  $k'_z$  axis and the apex of the cone is moving to the origin of the coordinates. To construct 3D images, (18) can still be used except that  $k'_z$  has a new definition. However, (19) should be modified to:

$$f(\vec{r}) \approx \frac{c^2}{(2\pi)^3} \int_0^\infty k^2 dk \int_{-\pi}^\pi d\theta \int_0^{\pi/2} \sin \zeta (1 - \cos \zeta) d\zeta \tilde{R}_{k,\zeta,\theta}^{(\text{T})'}(\omega) e^{-ikr \sin \zeta \cos(\phi-\theta) - ik(\cos \zeta - 1)z}, \quad (46)$$

where the superscript “(T)” means “transmission” and  $\tilde{R}_{k,\zeta,\theta}^{(\text{T})'}(\omega) = \tilde{R}_{k_x,k_y,k_z}^{(\text{T})}(\omega)$  is the temporal Fourier transform of the received signal. 2D B-mode transmission images can also be constructed with formulas similar to (29) to (36) with the new  $k'_z$  mentioned above. It is important to know that the Fourier space coverage implied by (46) is much smaller and incomplete as compared to those shown in Fig. 2 because the top of the half spheres is always at the origin of coordinates no matter what radii of the spheres are and the spheres are not rotated around the origin. In addition, (46) is only valid for waves scattered from objects and thus the direct incident wave should be removed from the received signals. Moreover, transmission imaging usually suffers from multiple reflections between transmitter and receiver. To obtain a more complete coverage of the Fourier space, the transducers should be rotated  $360^\circ$  around the objects (monochromatic waves can be used). This is the traditional transmission tomography [55] and may have severe image registration problem if the speed of sound of objects is not uniform in all directions.

#### L. Interpolation-Free Versus Fourier-Domain Interpolation

Image construction formulas such as (19) can be evaluated directly with numerical integrations without any interpolations. This is because the parameters,  $k_x$  and  $k_y$ , of limited diffraction array beam can be calculated from (8) for equal-space sampling along  $\theta$  and  $\zeta$ . Temporal FFT gives samples directly at the equal-space intervals of  $k$ . However, numerical integrations are slow and the nonuniform sampling in the  $(k_x, k_y, k'_z)$ -space requires more samples to achieve the same quality in image construction [67].

To speed up the image construction, spatial Fourier transform of the object functions at the rectangular grids

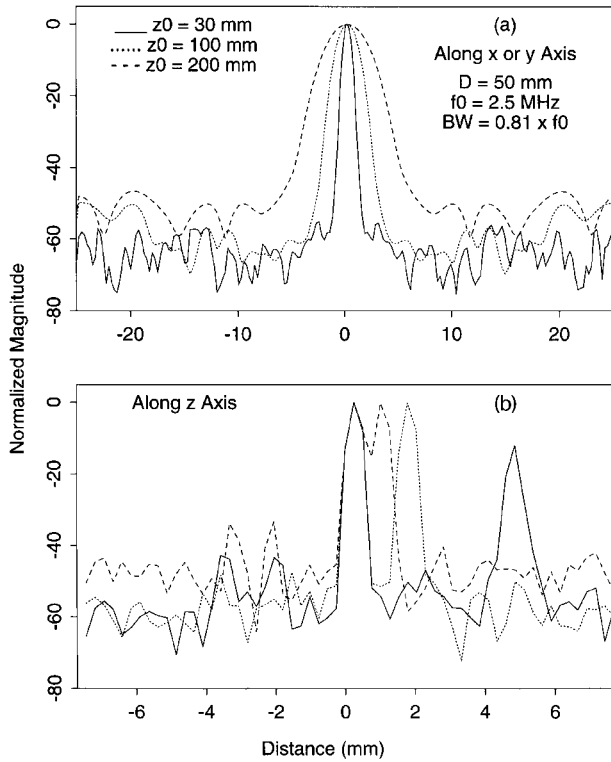


Fig. 8. (a) Lateral line plots of constructed 3D images of the point scatterer in the middle layer of the three-layer object along the  $x$  axis at three axial distances:  $z = 30$  (solid lines), 100 (dotted lines), and 200 mm (dashed lines). (b) Line plots of the constructed 3D images of the same point scatterer but along the  $z$  axis. The vertical axes are in dB scale.

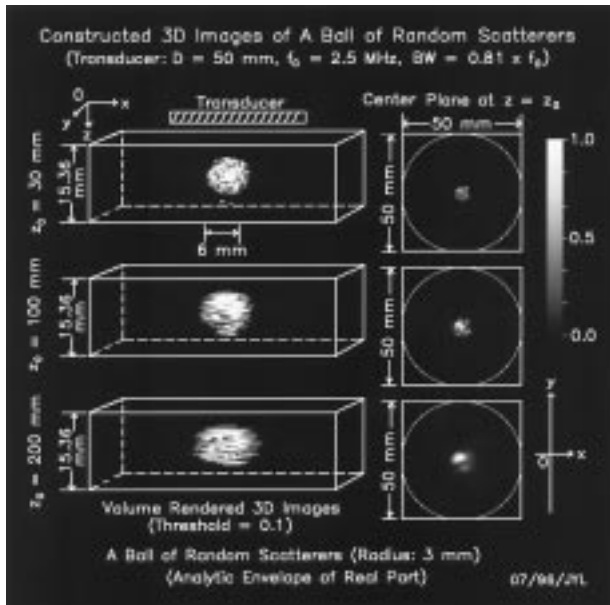


Fig. 9. Constructed 3D images of a sphere (3 mm radius) of random scatterers in Fig. 6(b). Panels in the left column are 3D volume rendered images with a threshold of 0.1 (maximum is 1.0). The size of constructed volumes is  $50 \times 50 \times 15.36 \text{ mm}^3$ . Transducer is assumed to be on top of the volumes. Transverse planes (parallel to the  $x-y$  plane) of the constructed images through the center of the sphere are shown on the right-hand side of the volume rendered images. Panels in the top, middle, and bottom rows correspond to the axial distances of the center of the sphere at  $z = 30, 100,$  and  $200 \text{ mm}$ , respectively.

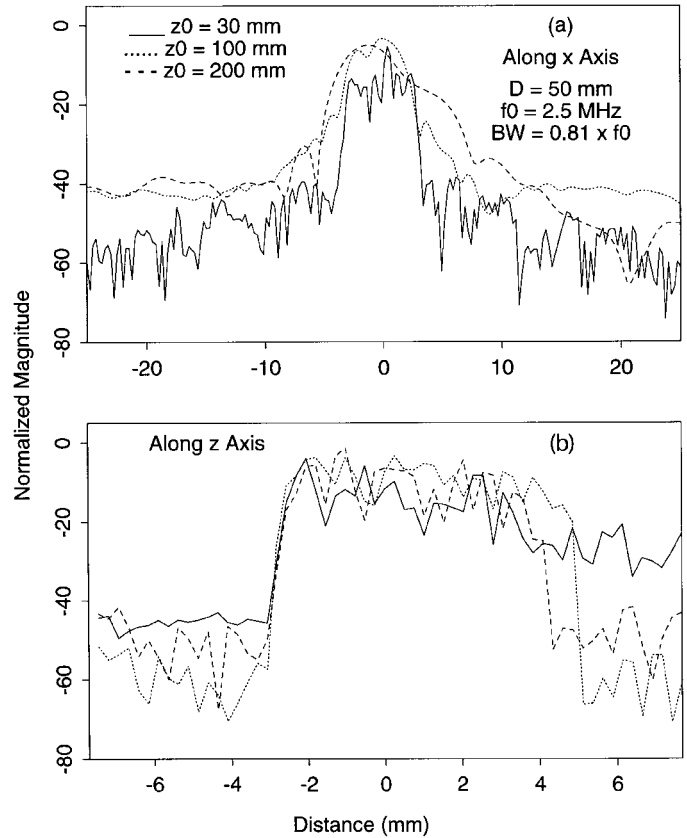


Fig. 10. (a) Lateral line plots through the center of the constructed 3D images of the sphere of random scatterers along the  $x$  axis at three axial distances:  $z = 30$  (solid lines), 100 (dotted lines), and 200 mm (dashed lines). (b) Line plots of the constructed images of the same sphere but along the  $z$  axis. The vertical axes are in dB scale.

of  $k_x$  and  $k_y$  is directly obtained by properly weighting the array transducers. The spatial Fourier transform at the equal-space intervals of  $k_z^2$  is then calculated with (40) using the nearest-neighbor interpolations [67]. After the spatial Fourier transform is known at all rectangular grids, 3D images are constructed with a 3D IFFT. This method has been used to construct all the images in this paper (Figs. 4, 7, 9, and 11).

#### M. Influence of Phase Aberration and Attenuation

The imaging method developed in this paper assumes that there are no attenuation and phase aberration in the objects. In addition, the objects are assumed to be composed of point scatterers of no multiple scattering. These conditions are similar to those assumed implicitly in all conventional B-scanners (beams can only be focused perfectly in media where there are no phase aberration, multiple scattering, and attenuation). Obviously, the new imaging method will work the best under these ideal conditions. Far away from these conditions, images are expected to degrade. In the following, the influence of the non-ideal conditions and methods for compensation are briefly discussed.

In commercial pulse-echo imaging systems, attenua-

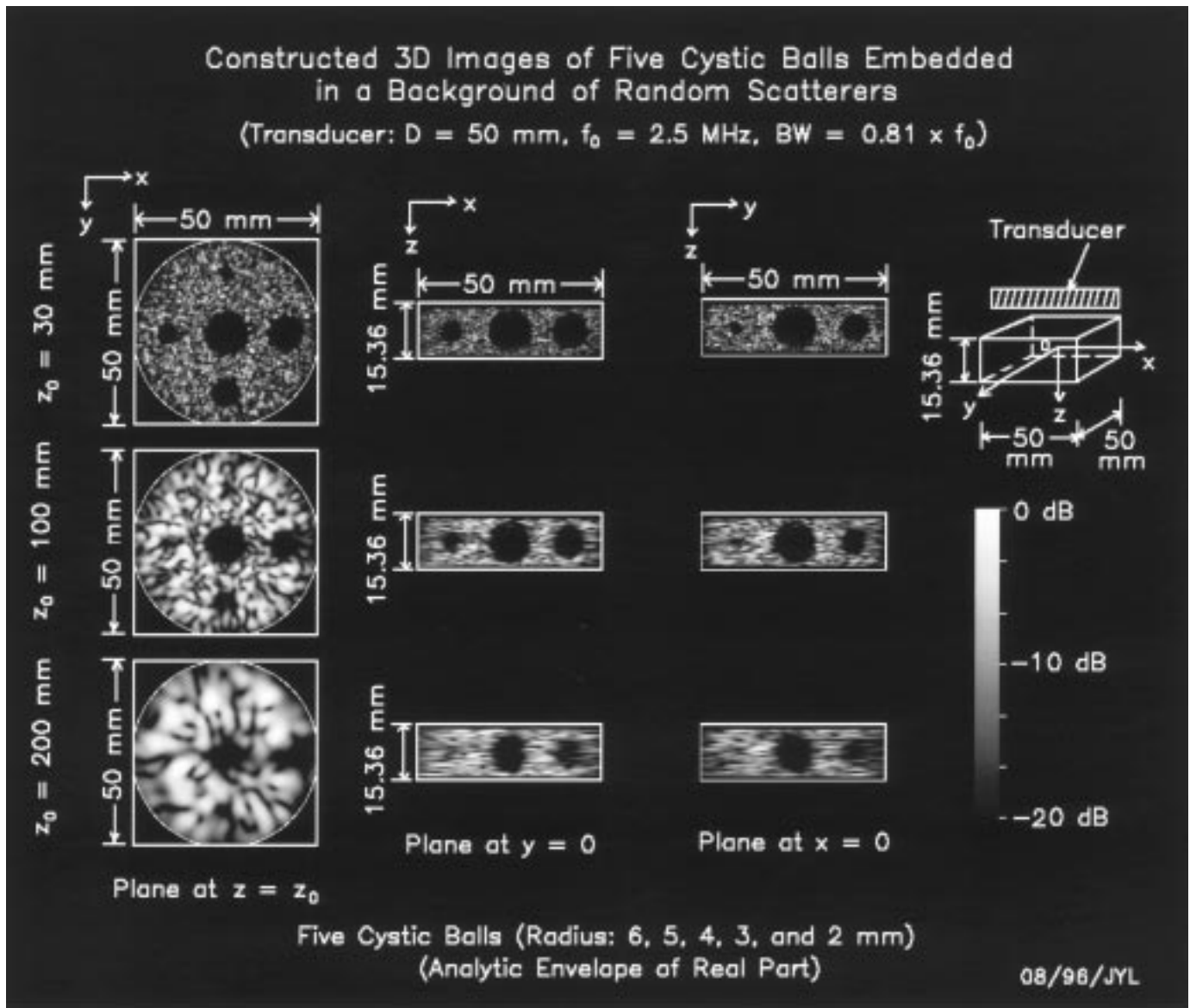
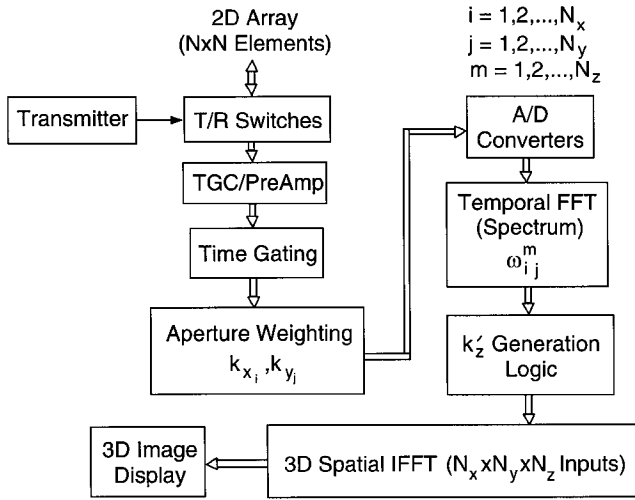


Fig. 11. Constructed 3D images of 5 cystic spheres (6, 5, 4, 3, and 2 mm in radius, respectively) embedded in a background of random scatterers [see Fig. 6(c)]. The size of constructed volumes is  $50 \times 50 \times 15.36$  mm<sup>3</sup>. Transducer is assumed to be on top of the volumes. Panels in the top, middle, and bottom rows correspond to the axial distances of the center of the central sphere at  $z = z_0 = 30, 100,$  and  $200$  mm, respectively. Panels in the left column represent the transverse planes (parallel to the  $x - y$  plane) of the constructed images at  $z = z_0$ . Panels in the middle column are constructed images in the  $x - z$  plane. And panels in the right column are in the  $y - z$  plane. The cross-sectional images are log compressed and the range is displayed from 0 to  $-20$  dB.

tion of acoustic waves in tissues are compensated with TGC (Fig. 12). The same technique can be applied to the new 2D and 3D pulse-echo imaging method. Frequency-dependent attenuation may cause the shift of temporal spectrum to lower frequencies. Like the conventional B-mode imaging, this may lower both lateral and axial resolutions when imaging tissues at a larger depth. Although we cannot avoid this problem, dynamic frequency technique that is used in commercial B-scanners can also be applied to the new method to increase signal-to-noise ratio. An experiment performed recently shows that the TGC works very well for both the conventional and new methods [56].

Phase aberration of biological soft tissues may cause

distortion to images. Influence of phase aberration depends on the size of transducers relative to its center wavelength, and the distance of objects from the transducer, etc. Currently, efforts have been made by many research groups to compensate for phase aberrations [68]. Techniques developed are also applicable to the new imaging method. In addition, restricting the Axicon angle,  $\zeta$ , in (19), (36), and other image construction formulas may also reduce the influence of phase aberration because objects are viewed within a smaller angle. However, as discussed before, smaller  $\zeta$  results in a lower lateral resolution. This is similar to the dynamic aperture technique used currently in commercial B-scanners to obtain images of approximately uniform resolutions over the entire depth



\* Note: Linear Electronic Delays can be Added if Steering is Desired.

Fig. 12. A suggested 3D imaging system for implementing the new method developed in this paper. For 2D B-mode imaging,  $k_y \equiv 0$  and a 1D array is used. In this case, aperture weightings are needed only along the  $x$  axis, and the spatial 3D IFFT is simplified to 2D [56]. (Notice that the A/D converters can also be moved to front of the block, "aperture weighting" or "time gating," in the diagram to digitize signal from each element. In this case, multichannel digital summations are required, which may increase system complexity.)

of interest (trade off lateral resolution near the surface of transducers with lower influence of phase aberration at these distances). An assessment of the influence of phase aberration on the new imaging method has been performed recently on data obtained from the experiment [57]. Results show that phase aberration has about the same influence on both the new and the conventional dynamic focusing (delay and sum) imaging methods.

#### N. Other Applications

The method developed in this paper could also be applied to electromagnetic (both broadband and narrow band) and optical (narrow band) imaging because electromagnetic waves satisfy the same scalar wave equations as the acoustic waves for most applications.

## VII. SUMMARY AND CONCLUSIONS

A new 2D and 3D pulse-echo imaging method (Fourier method) has been developed with limited diffraction beams. This method has a potential to achieve a high image frame rate (up to 3750 frames/s for biological soft tissues at a depth of 200 mm) and can be implemented with relatively simple and inexpensive hardware because the FFT and IFFT algorithms can be used. Computer simulation with the new method has been carried out to construct 2D C-mode, 2D B-mode, and 3D images on various types of objects. An experiment on an ATS 539 tissue equivalent phantom (attenuation coefficient is about

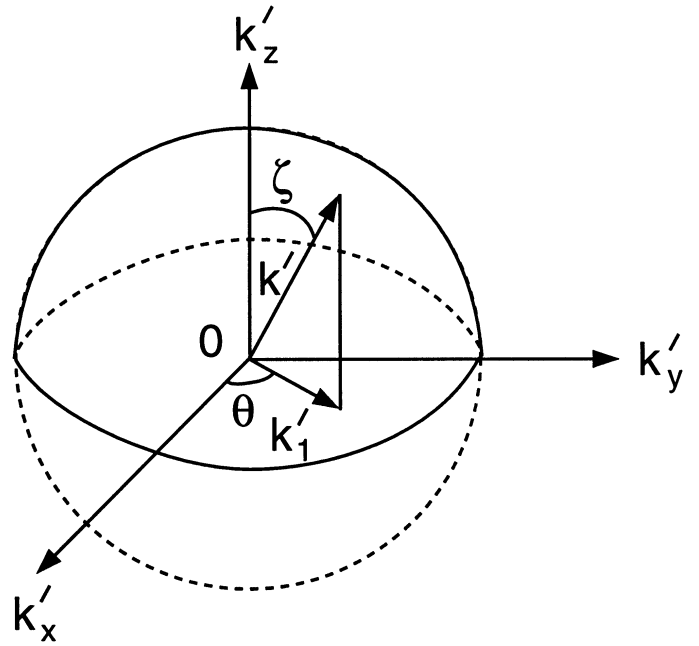


Fig. 13. Spatial Fourier domain coverage for imaging of radiation sources ( $k' = k$ ,  $k'_x = k_x$ ,  $k'_y = k_y$ ,  $k'_z = k_z$ ,  $k'_1 = k_1$ ) or for pulse-echo imaging using limited diffraction array beams in both transmission and reception ( $k' = 2k$ ,  $k'_x = 2k_x$ ,  $k'_y = 2k_y$ ,  $k'_z = 2k_z$ ,  $k'_1 = 2k_1$ ).

0.5 dB/MHz/cm) has been performed and 2D B-mode images have been constructed [56].

The results of the simulation and experiment have shown that the new imaging method is robust and is not sensitive to various limitations imposed by practical systems in medical ultrasound. The quality of images constructed with the new method is comparable to that obtained with the conventional dynamic focusing method (delay and sum [49]) in terms of spatial resolutions, sidelobes, signal-to-noise ratio, and contrast. A new study with the experiment data has demonstrated that the influence of phase aberration is about the same on both methods [57].

In addition, lateral resolution of images can be increased greatly if limited diffraction array beams are used in both transmission and reception (two-way imaging). In this case, a larger image field of view can be obtained without beam steering. Sidelobes of both the one-way (plane wave transmission) and two-way imaging systems can be reduced dramatically with an aperture weighting on limited diffraction array beams.

In conclusion, the new method is very promising for high frame rate multidimensional imaging with low motion artifacts. It could have an impact on future commercial imaging systems because of its simplicity and potentials for reduction of system cost. The new method can also be applied to nonmedical areas such as remote sensing and underwater acoustic imaging.

## ACKNOWLEDGMENTS

The author thanks Dr. James F. Greenleaf in the Department of Physiology and Biophysics, Mayo Clinic, for discussion of the work.

## REFERENCES

- [1] J. A. Stratton, *Electromagnetic Theory*. New York and London: McGraw-Hill Book Company, 1941, Page 356.
- [2] J. Durnin, "Exact solutions for nondiffracting beams. I. The scalar theory," *J. Opt. Soc. Amer. A*, vol. 4, no. 4, pp. 651–654, 1987.
- [3] J. Durnin, J. J. Miceli, Jr., and J. H. Eberly, "Diffraction-free beams," *Phys. Rev. Lett.*, vol. 58, pp. 1499–1501, Apr. 13, 1987.
- [4] J.-y. Lu, H.-h. Zou, and J. F. Greenleaf, "Biomedical ultrasound beam forming," *Ultrasound Med. Biol.*, vol. 20, pp. 403–428, July 1994.
- [5] G. Indebetow, "Nondiffracting optical fields: some remarks on their analysis and synthesis," *J. Opt. Soc. Amer. A*, vol. 6, pp. 150–152, Jan. 1989.
- [6] F. Gori, G. Guattari, and C. Padovani, "Model expansion for  $J_0$ -correlated Schell-model sources," *Opt. Commun.*, vol. 64, pp. 311–316, Nov. 15, 1987.
- [7] K. Uehara and H. Kikuchi, "Generation of near diffraction-free laser beams," *Appl. Physics B*, vol. 48, pp. 125–129, 1989.
- [8] L. Vicari, "Truncation of nondiffracting beams," *Opt. Commun.*, vol. 70, pp. 263–266, Mar. 15, 1989.
- [9] M. Zahid and M. S. Zubairy, "Directionality of partially coherent Bessel-Gauss beams," *Opt. Commun.*, vol. 70, pp. 361–364, Apr. 1, 1989.
- [10] J. Ojeda-Castaneda and A. Noyola-Iglesias, "Nondiffracting wavefields in grin and free-space," *Microwave Opt. Technol. Lett.* vol. 3, pp. 430–433, Dec. 1990.
- [11] D. K. Hsu, F. J. Margetan, and D. O. Thompson, "Bessel beam ultrasonic transducer: fabrication method and experimental results," *Appl. Phys. Lett.*, vol. 55, pp. 2066–2068, Nov. 13, 1989.
- [12] J. A. Campbell and S. Soloway, "Generation of a nondiffracting beam with frequency independent beam width," *J. Acoust. Soc. Amer.*, vol. 88, pp. 2467–2477, Nov. 1990.
- [13] J.-y. Lu, "Bowtie limited diffraction beams for low-sidelobe and large depth of field imaging," *IEEE Trans. Ultrason., Ferroelect., Freq. Contr.*, vol. 42, pp. 1050–1063, Nov. 1995.
- [14] —, "Producing bowtie limited diffraction beams with synthetic array experiment," *IEEE Trans. Ultrason., Ferroelect., Freq. Contr.*, vol. 43, pp. 893–900, Sept. 1996.
- [15] J.-y. Lu and J. F. Greenleaf, "Diffraction-limited beams and their applications for ultrasonic imaging and tissue characterization," in *New Developments in Ultrasonic Transducers and Transducer Systems*, F. L. Lizzi, Ed., Proceedings SPIE, vol. 1733, 1992, pp. 92–119.
- [16] J.-y. Lu, T. K. Song, R. R. Kinnick, and J. F. Greenleaf, "In vitro and in vivo real-time imaging with ultrasonic limited diffraction beams," *IEEE Trans. Med. Imag.*, vol. 12, pp. 819–829, Dec. 1993.
- [17] J.-y. Lu and J. F. Greenleaf, "Ultrasonic nondiffracting transducer for medical imaging," *IEEE Trans. Ultrason., Ferroelect., Freq. Contr.*, vol. 37, pp. 438–447, Sept. 1990.
- [18] J.-y. Lu and J. F. Greenleaf, "Pulse-echo imaging using a nondiffracting beam transducer," *Ultrasound Med. Biol.*, vol. 17, pp. 265–281, May 1991.
- [19] J.-y. Lu and J. F. Greenleaf, "Evaluation of a nondiffracting transducer for tissue characterization," *Proc. IEEE Ultrason. Symp.*, 90CH2938–9, vol. 2, 1990, pp. 795–798.
- [20] J.-y. Lu, "Improving accuracy of transverse velocity measurement with a new limited diffraction beam," *Proc. IEEE Ultrason. Symp.*, 96CH35993, vol. 2, 1996, pp. 1255–1260.
- [21] J.-y. Lu, X.-L. Xu, H.-h. Zou, and J. F. Greenleaf, "Application of Bessel beam for Doppler velocity estimation," *IEEE Trans. Ultrason., Ferroelect., Freq. Contr.*, vol. 42, pp. 649–662, July 1995.
- [22] J.-y. Lu, "High-speed transmissions of images with limited diffraction beams," in *Acoustical Imaging*, vol. 23, S. Lee, Ed., Proc. 23rd Int. Symp. Acoust. Imaging, Boston, MA, Apr. 13–16, 1997, (In Press).
- [23] J.-y. Lu and J. F. Greenleaf, "Producing deep depth of field and depth-independent resolution in NDE with limited diffraction beams," *Ultrason. Imaging*, vol. 15, pp. 134–149, April 1993.
- [24] J.-y. Lu and J. F. Greenleaf, "Nondiffracting X waves—exact solutions to free-space scalar wave equation and their finite aperture realizations," *IEEE Trans. Ultrason., Ferroelect., Freq. Contr.*, vol. 39, pp. 19–31, Jan. 1992.
- [25] J.-y. Lu and J. F. Greenleaf, "Experimental verification of nondiffracting X waves," *IEEE Trans. Ultrason., Ferroelect., Freq. Contr.*, vol. 39, pp. 441–446, May 1992.
- [26] J. Fagerholm, A. T. Friberg, J. Huttunen, D. P. Morgan, and M. M. Salomaa, "Angular-spectrum representation of nondiffracting X waves," *Phys. Rev. E*, vol. 54, pp. 1–6, Oct. 1996.
- [27] T. K. Song, J.-y. Lu and J. F. Greenleaf, "Modified X waves with improved field properties," *Ultrason. Imaging*, vol. 15, pp. 36–47, Jan. 1993.
- [28] J.-y. Lu and J. F. Greenleaf, "Formation and propagation of limited diffraction beams," *Acoust. Imaging*, vol. 20, Y. Wei and B.-l. Gu, Ed., pp. 331–343, 1993.
- [29] J.-y. Lu, "Limited diffraction array beams," *Int. J. Imaging Syst. Technol.*, vol. 8, pp. 126–136, Jan. 1997.
- [30] —, "Designing limited diffraction beams," *IEEE Trans. Ultrason., Ferroelect., Freq. Contr.*, vol. 44, pp. 181–193, Jan. 1997.
- [31] —, "Construction of limited diffraction beams with Bessel bases," *Proc. IEEE Ultrason. Symp.*, 95CH35844, vol. 2, 1995, pp. 1393–1397.
- [32] J.-y. Lu, H.-h. Zou, and J. F. Greenleaf, "A new approach to obtain limited diffraction beams," *IEEE Trans. Ultrason., Ferroelect., Freq. Contr.*, vol. 42, pp. 850–853, Sept. 1995.
- [33] J.-y. Lu and J. F. Greenleaf, "A study of two-dimensional array transducers for limited diffraction beams," *IEEE Trans. Ultrason., Ferroelect., Freq. Contr.*, vol. 41, pp. 724–739, Sept. 1994.
- [34] J.-y. Lu and J. F. Greenleaf, "Sidelobe reduction for limited diffraction pulse-echo systems," *IEEE Trans. Ultrason., Ferroelect., Freq. Contr.*, vol. 40, pp. 735–746, Nov. 1993.
- [35] J. N. Brittingham, "Focus wave modes in homogeneous Maxwell's equations: transverse electric mode," *J. Appl. Phys.*, vol. 54, no. 3, pp. 1179–1189, 1983.
- [36] R. W. Ziolkowski, "Exact solutions of the wave equation with complex source locations," *J. Math. Phys.*, vol. 26, pp. 861–863, Apr. 1985.
- [37] R. W. Ziolkowski, D. K. Lewis, and B. D. Cook, "Evidence of localized wave transmission," *Phys. Rev. Lett.*, vol. 62, pp. 147–150, Jan. 9, 1989.
- [38] E. Heyman, B. Z. Steinberg, and L. B. Felsen, "Spectral analysis of focus wave modes," *J. Opt. Soc. Amer. A*, vol. 4, pp. 2081–2091, Nov. 1987.
- [39] R. Donnelly, D. Power, G. Templeman, and A. Whalen, "Graphic simulation of superluminal acoustic localized wave pulses," *IEEE Trans. Ultrason., Ferroelect., Freq. Contr.*, vol. 41, no. 1, pp. 7–12, 1994.
- [40] J.-y. Lu and J. F. Greenleaf, "Comparison of sidelobes of limited diffraction beams and localized waves," *Acoust. Imaging*, vol. 21, J. P. Jones, Ed., pp. 145–152, 1995.
- [41] J.-y. Lu, "Limited diffraction beams for high frame rate 2D and 3D pulse-echo imaging," *J. Ultrasound Med.* vol. 16, no. 3, March, 1997. Proc. AIUM 41st Annu. Conv., San Diego, CA, March 23–26, 1997 (Abst.).
- [42] L. N. Bohs, B. H. Friemel, B. A. McDermott, and G. E. Trahey, "A real-time system for quantifying and displaying two-dimensional velocities using ultrasound," *Ultrasound Med. Biol.*, vol. 19, no. 9, pp. 751–761, 1993.
- [43] F. Ollivier, P. Alais, and P. Cervenka, "A high resolution bathymetric sidescan sonar using dynamic focusing and beam steering," *Acoust. Imaging*, vol. 22, P. Tortoli, Ed., pp. 573–582, 1996.
- [44] D. P. Shattuck, M. D. Weinschenker, S. W. Smith, and O. T. von Ramm, "Explososcan: A parallel processing technique for high speed ultrasound imaging with linear phased arrays," *J. Acoust. Soc. Amer.*, vol. 75, no. 4, pp. 1273–1282, 1984.
- [45] S. W. Smith, H. G. Pavy, Jr., and O. T. von Ramm, "High-speed ultrasound volumetric imaging system—Part I: Transducer design and beam steering," *IEEE Trans. Ultrason., Ferroelect., Freq. Contr.*, vol. 38, pp. 100–108, Mar., 1991.
- [46] O. T. von Ramm, S. W. Smith, and H. G. Pavy, Jr., "High-speed ultrasound volumetric imaging system—Part II: Parallel

- processing and image display," *IEEE Trans. Ultrason., Ferroelect., Freq. Contr.*, vol. 38, pp. 109–115, Mar., 1991.
- [47] P. N. T. Wells, *Biomedical Ultrasonics*. New York: Academic, Ch. 2–6.
- [48] M. Karaman, P.-C. Li, and M. O'Donnell, "Array processing for hand-held scanners," *Proc. IEEE Ultrason. Symp.*, 94CH3468–6, vol. 3, 1994, pp. 1543–1546.
- [49] J. Shen, H. Wang, C. Cain, and E. S. Ebbini, "A post-beamforming processing technique for enhancing conventional pulse-echo ultrasound imaging contrast resolution," in *Proc. IEEE Ultrason. Symp.*, 95CH35844, vol. 2, 1995, pp. 1319–1322.
- [50] E. S. Ebbini, "Optimal transversal filter bank for 3D real-time acoustical imaging," *Proc. Twenty-Sixth Asilomar Conference on Signals, Systems and Computers*, vol. 2, pp. 831–835, 1992.
- [51] S. J. Norton and M. Linzer, "Ultrasonic reflectivity imaging in three dimensions: exact inverse scattering solutions for plane, cylindrical, and spherical apertures," *IEEE Trans. Biomed. Eng.*, vol. BME-28, pp. 202–220, Feb. 1981.
- [52] D. Hiller and H. Ermert, "System analysis of ultrasound reflection mode computerized tomography," *IEEE Trans. Sonics Ultrason.*, vol. SU-31, pp. 240–250, July 1984.
- [53] B. A. Roberts and A. C. Kak, "Reflection mode diffraction tomography," *Ultrason. Imaging*, vol. 7, pp. 300–320, Oct. 1985.
- [54] S. A. Johnson, J. F. Greenleaf, M. Tanaka, B. Rajagopalan, and R. C. Bahn, "Reflection and transmission techniques for high resolution quantitative synthesis of ultrasound parameter images," *Proc. IEEE Ultrason. Symp.*, 77CH1264-ISU, 1977, pp. 983–988.
- [55] R. K. Mueller, M. Kaveh, and G. Wade, "Reconstructive tomography and applications to ultrasonics," *Proc. IEEE*, vol. 67, pp. 567–587, Apr. 1979.
- [56] J.-y. Lu, "Experimental study of high frame rate imaging with limited diffraction beams," *IEEE Trans. Ultrason., Ferroelect., Freq. Contr.*, submitted for publication.
- [57] —, "Assessment of phase aberration effects on high frame rate imaging," *Ultrason. Imaging*, vol. 19, April, 1997 (Abst).
- [58] C. B. Burckhardt, H. Hoffmann, and P. A. Grandchamp, "Ultrasound axicon: a device for focusing over a large depth," *J. Acoust. Soc. Amer.*, vol. 54, pp. 1628–1630, Dec. 1973.
- [59] F. S. Foster, M. S. Patterson, M. Arditi, and J. W. Hunt, "The conical scanner: a two transducer ultrasound scatter imaging technique," *Ultrason. Imaging*, vol. 3, pp. 62–82, Apr. 1981.
- [60] P. M. Morse and H. Feshbach, *Methods of Theoretical Physics, Part I*, New York: McGraw-Hill, 1953, p. 620.
- [61] R. Bracewell, *The Fourier Transform and its Applications*. New York: McGraw-Hill, 1965, Ch. 4 and 6.
- [62] A. V. Oppenheim and R. W. Schaffer, *Digital Signal Processing*, Englewood Cliffs, NJ: Prentice-Hall, 1975, Ch. 1 and 5.
- [63] F. John, *Partial Differential Equations*. New York: Springer-Verlag, 1982, p. 12.
- [64] J. W. Goodman, *Introduction to Fourier Optics*. New York: McGraw-Hill, 1968, Ch. 2–4.
- [65] D. R. Bailes and D. J. Bryant, "NMR imaging," *Contemp. Phys.*, vol. 25, pp. 441–475, 1984.
- [66] M. J. Bronskill and P. Sprawls, *The Physics of MRI—1992 AAPM Summer School Proceedings*. Woodbury, NY: American Institute of Physics, 1993.
- [67] J.-y. Lu, "A computational study for synthetic aperture diffraction tomography: Interpolation versus interpolation-free," *Acoust. Imaging*, vol. 16, L. W. Kessler, Ed., pp. 421–443, 1988.
- [68] S. W. Flax and M. O'Donnell, "Phase aberration correction using signals from point reflectors and diffuse scatterers: basic principles," *IEEE Trans. Ultrason., Ferroelect., Freq. Contr.*, vol. 35, no. 6, pp. 758–767, 1988.
- [69] M. Soumekh, "Array imaging with beam-steered data," *IEEE Trans. Image Processing*, vol. 1, no. 3, pp. 379–390, July, 1992.
- [70] J. T. Ylitalo and H. Ermert, "Ultrasound synthetic aperture imaging: monostatic approach," *IEEE Trans. Ultrason., Ferroelect., Freq. Contr.*, vol. 41, no. 3, pp. 333–339, May, 1994.



**Jian-yu Lu** (M'88) was born in Fuzhou, Fujian Province, People's Republic of China. He received the B.S. degree in electrical engineering in February 1982 from Fudan University, Shanghai, China; the M.S. degree in 1985 from Tongji University, Shanghai, China; and the Ph.D. degree in 1988 from Southeast University, Nanjing, China.

He is currently an Associate Professor of Biophysics at the Mayo Medical School and an Associate Consultant at the Department of Physiology and Biophysics, Mayo Clinic/Foundation, Rochester, MN. From March 1990 to December 1991, he was a Research Associate at the Department of Physiology and Biophysics, and from December 1988 to February 1990, he was a postdoctoral Research Fellow there. Prior to that, he was a faculty member of the Department of Biomedical Engineering, Southeast University, Nanjing, China, and worked with Prof. Yu Wei. His research interests are in acoustic imaging and tissue characterization, medical ultrasonic transducers, and ultrasonic beam forming and propagation.

Dr. Lu is a recipient of the Outstanding Paper Award for two papers published in the 1992 IEEE Transactions on the UFFC, a recipient of the Edward C. Kendall Award from the Mayo Alumni Association, Mayo Foundation in 1992. He also received both the FIRST Award from the NIH and the Biomedical Engineering Research Grant Award from the Whitaker Foundation in 1991. He is a member of the IEEE UFFC Society, the American Institute of Ultrasound in Medicine, and Sigma Xi.